LLMs-Powered Accurate Extraction, Querying and Intelligent Management of Literature-derived 2D Materials Data

Lijun Shang^{1,2}, Yadong Yu^{1,*}, Wenqiang Kang^{1,2}, Jian Zhou³, Dongyue Gao², Pan Xiang¹, Zhe Liu¹,

Mengyan Dai^{1,*}, Zhonglu Guo², Zhimei Sun^{3,*}

¹Chemical Defense Institute, Academy of Military Sciences, Beijing 102205, China.

²Hebei Key Laboratory of Boron Nitride Micro and Nano Materials, School of Materials Science and Engineering, Hebei University of Technology, Tianjin 300130, China.

³School of Materials Science and Engineering, and Center for Integrated Computational Materials Science, International Research Institute for Multidisciplinary Science, Beihang University, Beijing 100191, P. R. China.

^{*}Correspondence and requests for materials should be addressed to Y. D. Yu or M. Y. Dai or Z. M. Sun: ydyu16@buaa.edu.cn, daidecai0558@163.com, zmsun@buaa.edu.cn.

Abstract

Two-dimensional (2D) materials have showed widespread applications in energy storage and conversion owning to their unique physicochemical, and electronic properties. Most of the valuable information for the materials, such as their properties and preparation methods, is included in the published research papers. However, due to the dispersion of synthetic sources and the inconsistency of performance reported in the literature, the data in the literature is difficult to be reused, thereby limiting the further research and progress of 2D materials. To this end, we proposed an end-to-end framework that couples large language models (LLMs) with domain informed context engineering and lightweight fine-tuning to extract structured knowledge at large-scale from the published papers, and then the knowledge is available externally through an agent-assisted data management system. As a result, the literature is collected via programmatic discovery and converted to standardized plain text, where the synthesis details, performance metrics, and article metadata are all included. We have applied the workflow to about 50,000 papers, curating 600,200 performance and 202,300 synthesis records. Compared with prompt-only extraction, context engineering has significantly improved the precision and recall, and fine-tuning can further increase the coverage of domain terminology. These data have been structured into a relational knowledge base with natural-language retrieval and guarded SQL execution. It achieves nearly perfect accuracy in simple and moderately complex queries, and can also achieve a relatively high accuracy even in complex multi-table queries. This work demonstrates how LLMs accelerate dataset construction, enable reproducible benchmarking, and support synthesis pathway design for 2D materials.

Keywords: Two-dimensional materials, Data mining, Context engineering, Large language models, Fine-tuning.

1. Introduction

In recent years, Two-dimensional (2D) materials have garnered significant interest due to their unique properties including physical, chemical, and electronic properties[1-5]. To date, a variety of 2D materials such as 2D transition metal carbides and nitrides (MXenes), 2D transition metal borides (MBenes), transition metal dichalcogenides (TMDs) and hexagonal boron nitride (hBN) have been discovered and successfully employed in various applications including energy storage and conversion and CO₂ reduction catalysis, flexible electronics and assorted photonic devices, and seawater desalination and water-purification membranes for environmental remediation[6-10]. However, in most cases, 2D materials data are limited in practical use due to the lack of complete synthetic provenance and high-quality characterization datasets[11, 12]. To further amplify 2D materials dataset. Campi et al. expanded the Materials Cloud 2D database under an extended high-throughput exfoliation-screening framework with DFT validation, obtaining 3,077 monolayers in total, including 2,004 that are easily exfoliable. Similarly, Momeni et al. mentioned that utilizing high-throughput screening and integrating experimental validation methods to expand the dataset for 2D materials[13, 14]. Extensive studies in this domain are mainly focused on employing high-throughput computational screening or experimental synthesis to augment datasets, but few reports have described expanding 2D materials datasets by mining data from published literature[15, 16], which possess a large amount of data. Compared with the time and resource intensive high-throughput computations or experimental syntheses, directly extracting validated results from previously published studies offers faster and more accurate 2D materials data. In the previous studies, Vaucher et al. built a transformer sequence-tosequence model to translate prose experimental procedures into structured, automation-ready action sequences. Pretrained on rule-based NLP outputs and refined with manual annotations, it achieved 60.8 percent exact sequence matches on a challenging test set; at thresholds of at least 90 percent and at least 75 percent, the match rates were 71.3 percent and 82.4 percent, respectively, demonstrating strong extraction precision for organic synthesis[17]. Tshitoyan et al. trained two-hundred-dimensional Word2vec embeddings on approximately 3.3 million materials-science abstracts for unsupervised literature mining, capturing periodic trends and structure-property relations. Using cosine similarity between material vectors and application keywords (for example, "thermoelectric"), the model retrospectively surfaced candidates not previously linked to the application: the top 50 predictions

were approximately eight times more likely to be studied within five years than randomly selected unstudied materials, and the rankings showed Spearman correlations of 0.59 with power factor and 0.52 with zT[18]. Jang et al. proposed a semi-supervised text mining method to extract synthesis and processing data, focusing on action sequences and parameters and using a small labeled corpus combined with unlabeled text to build a robust superalloy dataset[19]. Therefore, combining literature-extracted synthesis parameters with performance data for 2D materials into a dataset can improve data quality while expanding the database. However, most reported text-mining methods are restricted to domain-specific corpora. Additionally, the canonicalization pipelines required to standardize the extracted data are markedly time-consuming and inefficient[20, 21]. Even in the simplest case, all extraction parameters must be optimized simultaneously. The search-and-optimization cycle must then be restarted from scratch for each target attribute. Meanwhile, extraction precision depends on researchers fully understanding the data, which greatly slows the process. Therefore, building an ondemand method that pulls information from all materials-science papers remains a major challenge.

Nowadays, large language models (LLMs), propelled by rapid advances in artificial intelligence, are gaining significant attention as a powerful and flexible means of tackling the above issues[22]. In earlier studies, Zheng et al. developed a workflow utilizing ChatGPT as a collaborator for human chemists, extracting 26,257 distinct synthesis parameters of approximately 800 metal-organic frameworks from 228 articles[23]. Polak and Morgan proposed a similar workflow for metallic glasses and high entropy alloys, employing follow-up questions to GPT-4 to ensure correctness and address the issues of hallucinations with LLMs[24]. Yang et al. used a repeated questioning strategy with GPT-4 for bandgap values, demonstrating reduced error rates and a more extensive dataset than humancurated databases[25]. Similarly, Schmidt et al. systematically assessed LLMs for data extraction and confirmed their feasibility. However, LLMs achieve only about 70% precision on structured data extraction tasks within specific domains; on open-source small models, this figure is often even lower[26]. To confront this limitation, task-specific fine-tuning has come to the fore[27]. Wang et al. fine-tuned LLMs, enhancing their performance in chemical text mining tasks like compound recognition and reaction role labeling, with minimal data and high efficiency[28]. By applying finetuning techniques to LLMs and leveraging the rich literature on 2D materials, LLMs can rapidly extract and organize synthesis and performance data. In addition, the code generation ability of LLMs makes

them promising methods for database management. Therefore, it is worth noting that combining LLMs with domain-specific adaptation can markedly enhance the speed and precision of 2D materials database construction and upkeep. Yet a full end-to-end workflow—from information extraction to database management—powered by LLMs has not yet been described to date.

In this study, we have investigated and integrated the LLM-powered 2D material information extraction technology to our proprietary data intelligent management platform. It enabled the construction of an application framework centered around an LLM agent, thereby achieving rapid retrieval, convenient access, and systematic analysis of 2D material information (as shown in Fig. 1). To begin with, literature is collected via OpenAlex using 2D material keywords or curated DOI lists to obtain download links (Fig. 1a). The collected corpus is compiled into a 2D materials text database and segmented by the Segment Any Text (SaT) model, producing standardized input files[29]. Notably, 3 000 manually annotated samples are used to fine-tune a model dedicated to extracting 2D materials information. In addition, in view of prompt sensitivity, context engineering has been introduced to allowing the model to utilize structured cues to precisely retrieve synthesis and property data, thereby improving extraction precision[30]. Finally, step-by-step extraction of article titles, Digital Object Identifiers (DOIs), synthesis details, and performance data is achieved by pairing the fine-tuned model with tailored prompts and structured input files[31] (Fig. 1b). By combining LLM fine-tuning on limited labeled data with prompt engineering, we have successfully resolved the performance degradation encountered when deploying smaller models for information extraction in the 2D materials domain. The performance of the extracted results in extraction precision has approached toptier open-source or closed-source models such as DeepSeek V3, Qwen3-235B-A22B, and Gemini 2.5 Flash[32, 33]. For effective data management, search, and analysis, the LLM-based data intelligent management system has integrated a set of intelligent agents that let users retrieve information from the database using natural language. The system also learns over time: repeated queries deepen its understanding of the database structure, steadily improving the precision and sophistication of data extraction (Fig. 1c). This integrated framework provides a foundation for accelerating materials discovery, with potential extensions to other emerging material systems and integration with automated experimental workflows for closed-loop materials development.

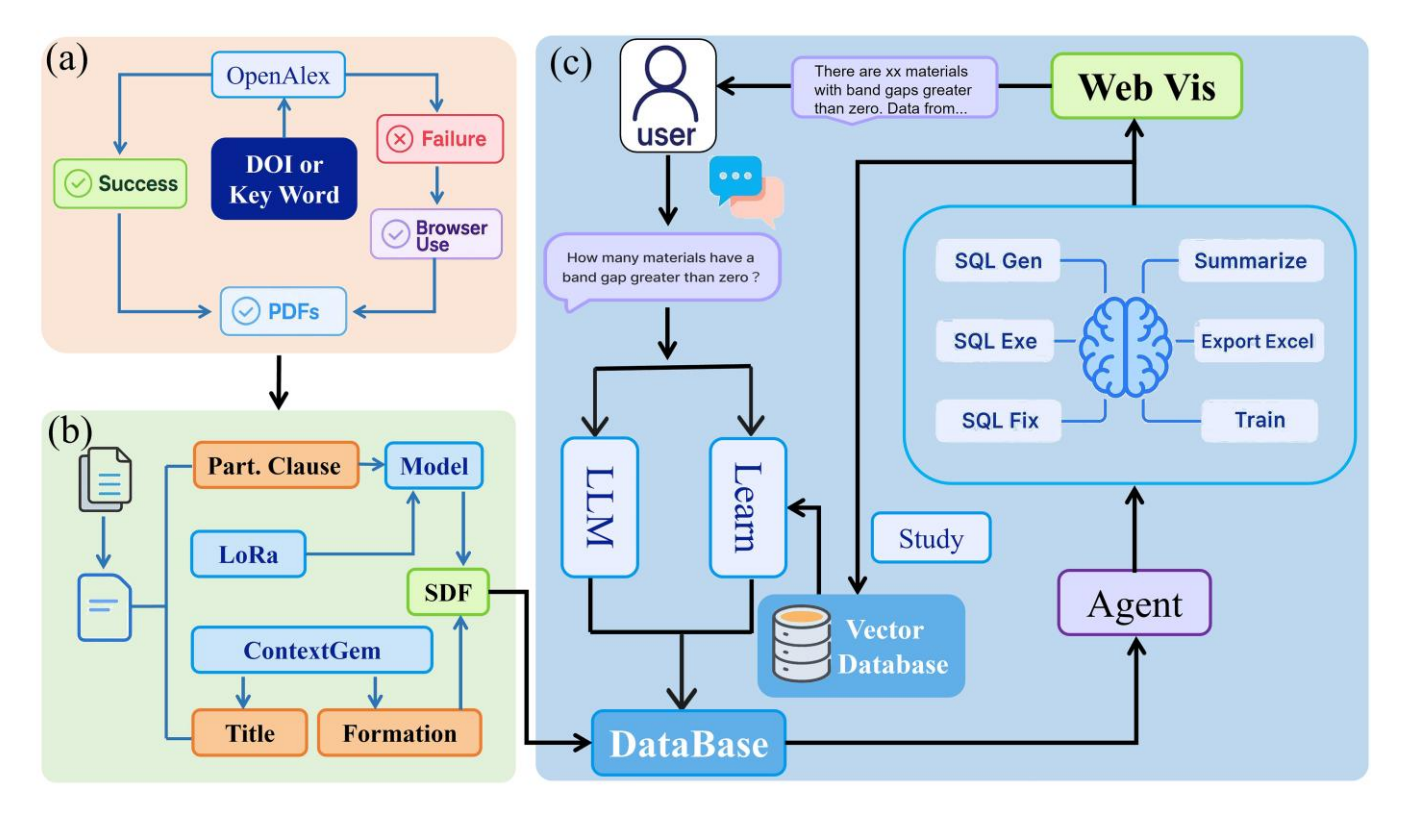


Fig. 1. Overall workflow of the literature collection and structured database construction. The pipeline comprises three stages: (a) literature retrieval and download; (b) literature processing and information extraction; and (c) the basic operating workflow of the data intelligent management system.

2. Results and discussion

2.1 Literature download and text structuring

In the literature download preparation stage, it is crucial to judge whether the literature's topic focuses on 2D materials. To ensure the accurate downloading of relevant literature, we first collected over 134,000 literature entries related to 2D materials, covering essential details such as authors, publication sources, publication years, and DOIs. As shown in Fig. 2a, first, OpenAlex was utilized to retrieve open-access paper download links based on the DOIs obtained above. This was supplemented by keyword-based searches to acquire additional relevant literature. Using a combination of link access and manual downloading, over 50,000 initially screened PDF documents related to 2D materials were obtained. To ascertain the validity of the corpus, we randomly sampled 1,000 documents and evaluated their relevance with three LLMs (GPT-4.1-mini, Gemini 2.5 Flash, and DeepSeek-R1). As shown in

Fig. 2b, over 95% of the sampled documents were judged to be related to 2D materials. Further analysis (Fig. 2c) showed that graphene constituted the largest share (37.5%), followed by TMDs (23.8%) and MXenes (20%), whereas h-BN accounted for only 0.84%. Given possible errors in model classification, we kept all 50,000 documents to reduce false negatives for extraction and analysis. Subsequent, all collected PDFs were converted to text with MinerU, a document parsing tool designed for batch automated content extraction [34, 35]. The extracted texts were then standardized using the SaT model, which employs segmentation algorithms combined with semantic understanding to identify and normalize paragraph and sentence boundaries based on contextual meaning. Finally, this structured text-processing approach not only enables more accurate identification of target sentences or paragraphs during subsequent information extraction but also precisely indicates the exact positions of the extracted information within the corresponding sentences when results are returned. Through structured processing of the text, preparations are made for subsequent 2D material information extraction and the construction of a data intelligent management system.

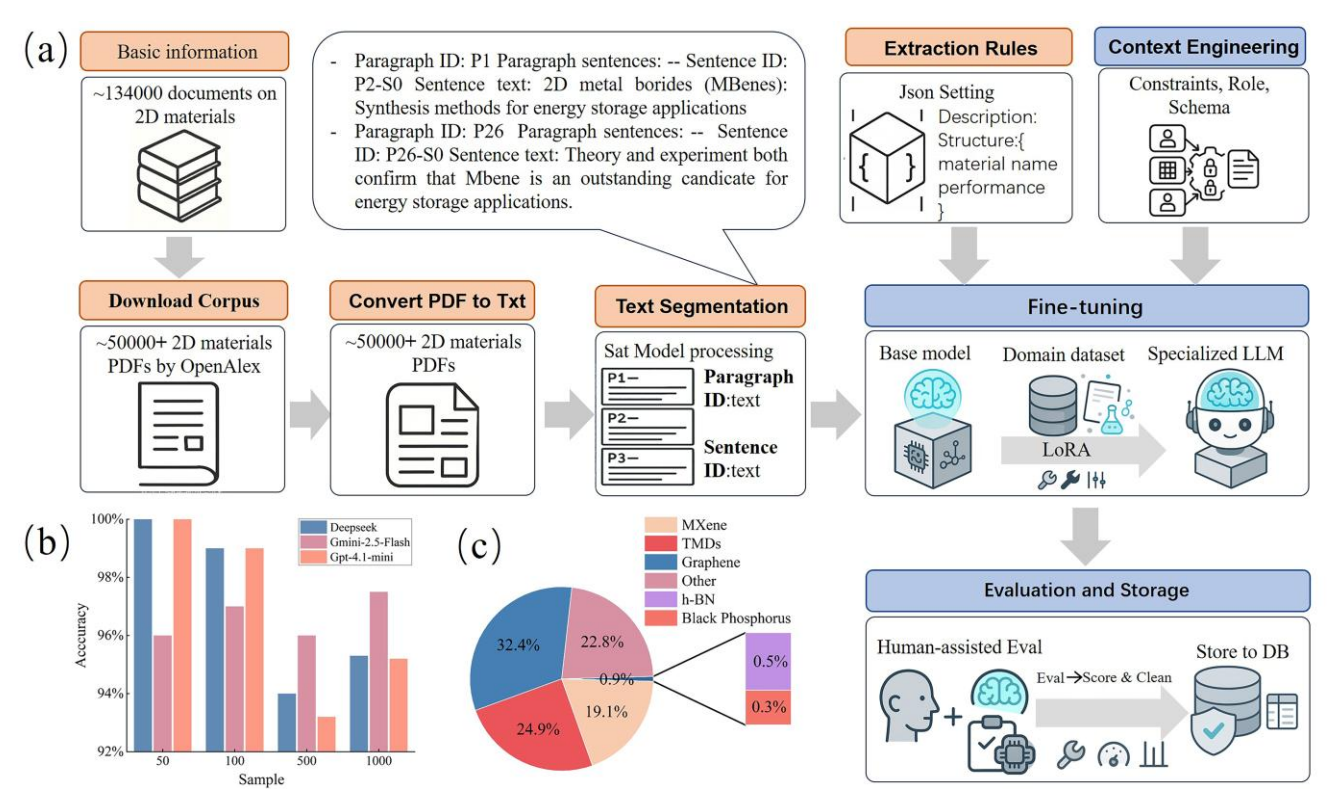


Fig. 2. Pipeline and results for processing 2D materials literature.(a) End-to-end workflow: download the corpus from OpenAlex; convert PDFs to text and perform sentence segmentation; construct a structured schema by combining extraction rules with context engineering; fine-tune the base model via LoRA; conduct human evaluation and then integrate into the database; (b) Bar chart showing the

proportion of papers classified as 2D materials-related by three models (DeepSeek, Gemini-2.5-Flash, GPT-4.1-mini) across different sample sizes (50, 100, 500, 1,000); (c) Pie chart illustrating the distribution of material types identified in the literature corpus.

2.2 Data extraction using large language models

Information data on 2D materials from a journal article can be extracted by leveraging the ability of LLMs to understand the specialized semantics of materials entities discussed in the text. However, obtaining the desired output from an LLM poses a challenging task and is presently a subject of active research. Even with the same prompt or instruction and text generation parameters, the LLMs can produce varying responses. This variation is even greater across different model, making response quality hard to predict. Simple natural language prompts do not always produce the expected results from LLMs, because these models interpret language in non-intuitive ways. Hence, tightening contextual constraints and adopting techniques and parameter settings that enforce a consistent response format to reduce stochastic variability are crucial. Equally crucial is targeted fine-tuning of smaller models, so that in the specific 2D materials domain they can approach the response quality of stronger models.

To address these issues, we no longer relied only on prompt engineering. Prompt-only approaches are sensitive to wording and order, leading to inconsistent results across different documents and runs. They also fail to ensure that the output matches the required JSON schema. Domain-specific synonyms and rare cases are poorly handled, which increases errors and reduces information coverage. To improve stability and consistency, we used context engineering to assign the model a fixed role as an information extractor which was responsible for extracting synthesis details, article metadata such as title and DOI, and materials performance, and by adding a simple, uniform JSON schema and rules on bottom of the information extractor, we could efficiently and accurately extract specific information. This approach provides stricter control over the model's behavior while maintaining extraction flexibility, producing consistent, structured results that are easy to verify. To assess gains in structural completeness and extraction precision from context engineering, we randomly sampled 1,000 documents and used three models, DeepSeek-V3, Qwen3-235B-A22B and Gemini-2.5-Flash. Each model ran under two settings, prompt engineering and context engineering. For both settings, we used

a bipartite matching method with a similarity threshold. The gold set is the human-annotated reference. TP is a predicted item that matches a gold item. FP is a predicted item that matches none. FN is a gold item that is not matched by any prediction. As shown in Fig. 3a, for text pairs, we used SequenceMatcher along with bigram-based and trigram-based Jaccard similarity to score each text block (see Supplementary Eq. (1) to (3))[36]. These scores were then combined through a weighted aggregation to produce the overall similarity for the pair. For numeric pairs, we computed similarity scores by comparing values directly, with the final score as a weighted sum of numeric components. When similarity exceeded a threshold (e.g., 0.65), we created an edge between gold and predicted items and applied one-to-one maximum matching to determine TP, FP, and FN, then calculated strict precision, recall, and F1. The one-to-one constraint penalizes outputs that merge several facts into one or segment too coarsely. In such cases a single prediction cannot cover multiple gold items, so recall and F1 may be underestimated. In Fig. 2b, context engineering markedly improves extraction success for both open-source models such as DeepSeek-V3 and closed-source models such as Gemini 2.5 Flash, reducing failure rates from about 30% to below 5% (as show in Supplementary Fig. S1). In addition to reliability gains, precision and recall also increase. For DeepSeek-V3, precision rises from 64% to 91% (up 27 percentage points, a 42% relative increase), and recall rises from 57% to 67% (up 10 percentage points, a 17% relative increase). These results indicate that context engineering is effective for materials information extraction.

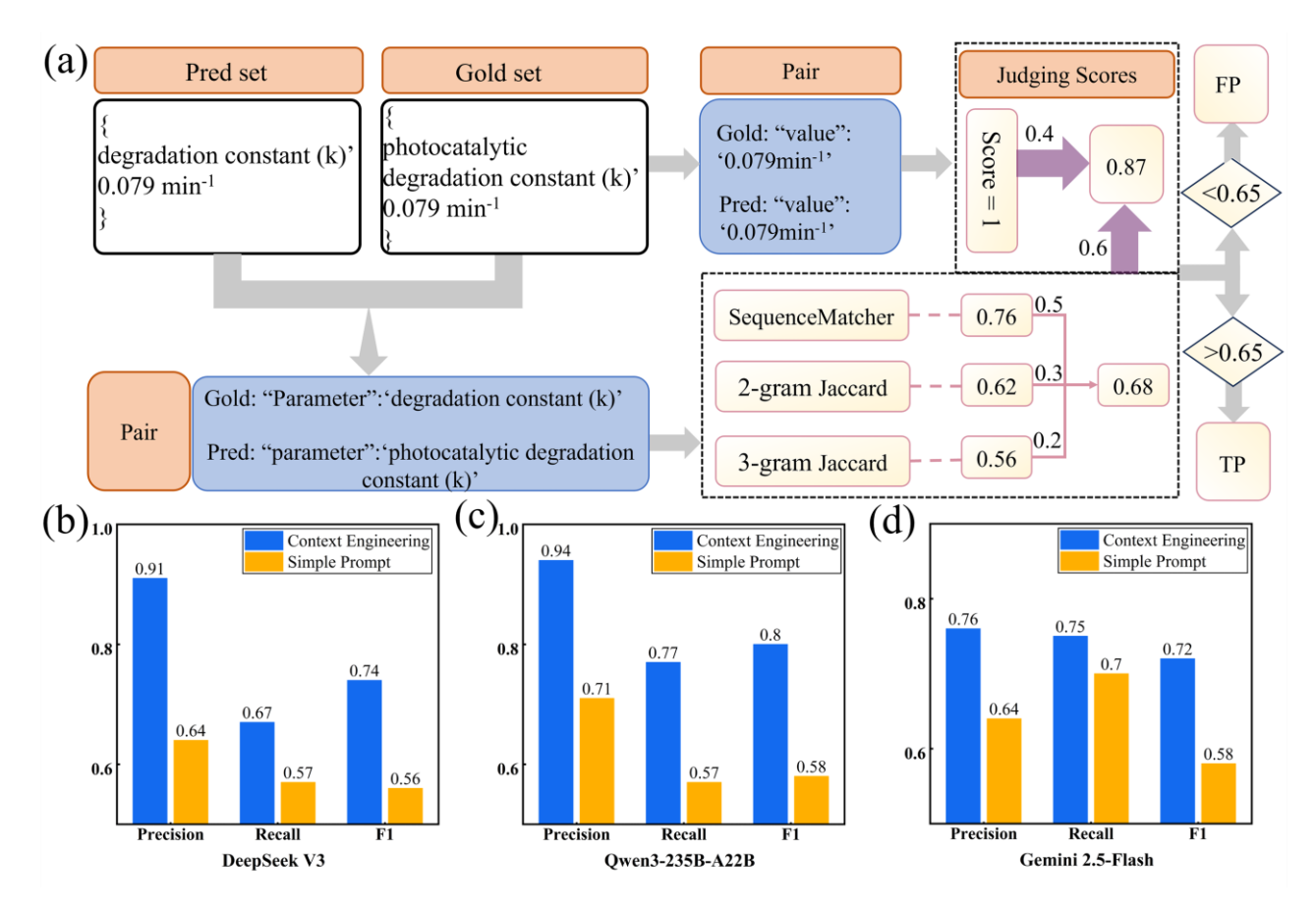


Fig. 3. Evaluation workflow and comparative results. (a) Schematic of the evaluation workflow for model-based information extraction;(b)–(d) Bar charts of the evaluation results (Precision, Recall, F1) for DeepSeek V3, Qwen3-235B-A22B, and Gemini-2.5-Flash under two settings: simple prompts and context engineering.

To push a smaller model toward or beyond higher-tier performance, we applied targeted adjustments. Foundation models freeze parameters after pretraining and cover limited domain knowledge, for example confusing MXenes or TMDs with specific materials, which compromises extraction quality. We curated a training dataset of 3,000 manually annotated examples and expanded it to 10,000 samples through paraphrase augmentation to enhance data diversity while maintaining annotation quality. For 2D-materials extraction task we chose parameter-efficient LoRA rather than full fine-tuning because our domain corpus is much smaller than the pretraining data, and full updates risk degrading existing abilities and raising memorization variants during fine-tuning, which reduces terminology ambiguity[37]. As shown in Fig. 4b, we monitored both training and validation losses throughout the fine-tuning process. The validation loss exhibited a minimum at 1,500 training steps,

after which it demonstrated an upward trend, signaling the onset of overfitting. Consequently, we selected the checkpoint at step 1,500 as our final extraction model to ensure optimal generalization performance. The fine-tuned model, combined with structural constraints from prompt engineering, improves field detection and hierarchical structures, achieving schema accuracy and extraction performance close to leading models. As illustrated in Fig. 4c, this approach achieved a precision of 0.83 and a recall of 0.66, demonstrating substantial improvements over the baseline. Subsequently, we then used the fine-tuned model to process over fifty thousand papers in batch. The results kept high output quality while reducing cost versus commercial models. Fig. 4d shows that extracting from two thousand papers costs \$26.78 with DeepSeek V3, \$23.79 with Qwen3-235B-A22B, and \$87.68 with Gemini-2.5-Flash. By contrast, our smaller model runs locally on a single RTX 4090, reducing total cost by about 90% while avoiding API-related data exposure. Finally, we extracted data from 50,000 papers and, prior to storage, ensured precision, stability, and utility through manual review and the removal of low-scoring or anomalous outputs, yielding a curated set of 600,200 performance records and 202,300 synthesis records, for which Supplementary Tables 1 and 2 present a subset. Based on this, we constructed a computable knowledge base for 2D materials. In an era where data value is paramount, this knowledge base can be used to fine-tune large models in the materials field or to build dedicated data foundations through Retrieval Augmented Generation (RAG)[38]. This approach enables rational design of synthesis pathways, parameter optimization, and accelerated discovery of new materials. Supported by high-quality, curated data, machine-learning models achieve improved generalization and transferability, while standardized experimental protocols exhibit greater comparability and reproducibility. Together, data and models shift materials research from experiencedriven practice to a data-guided workflow, transforming fragmented literature into structured, computable, and actionable data assets.

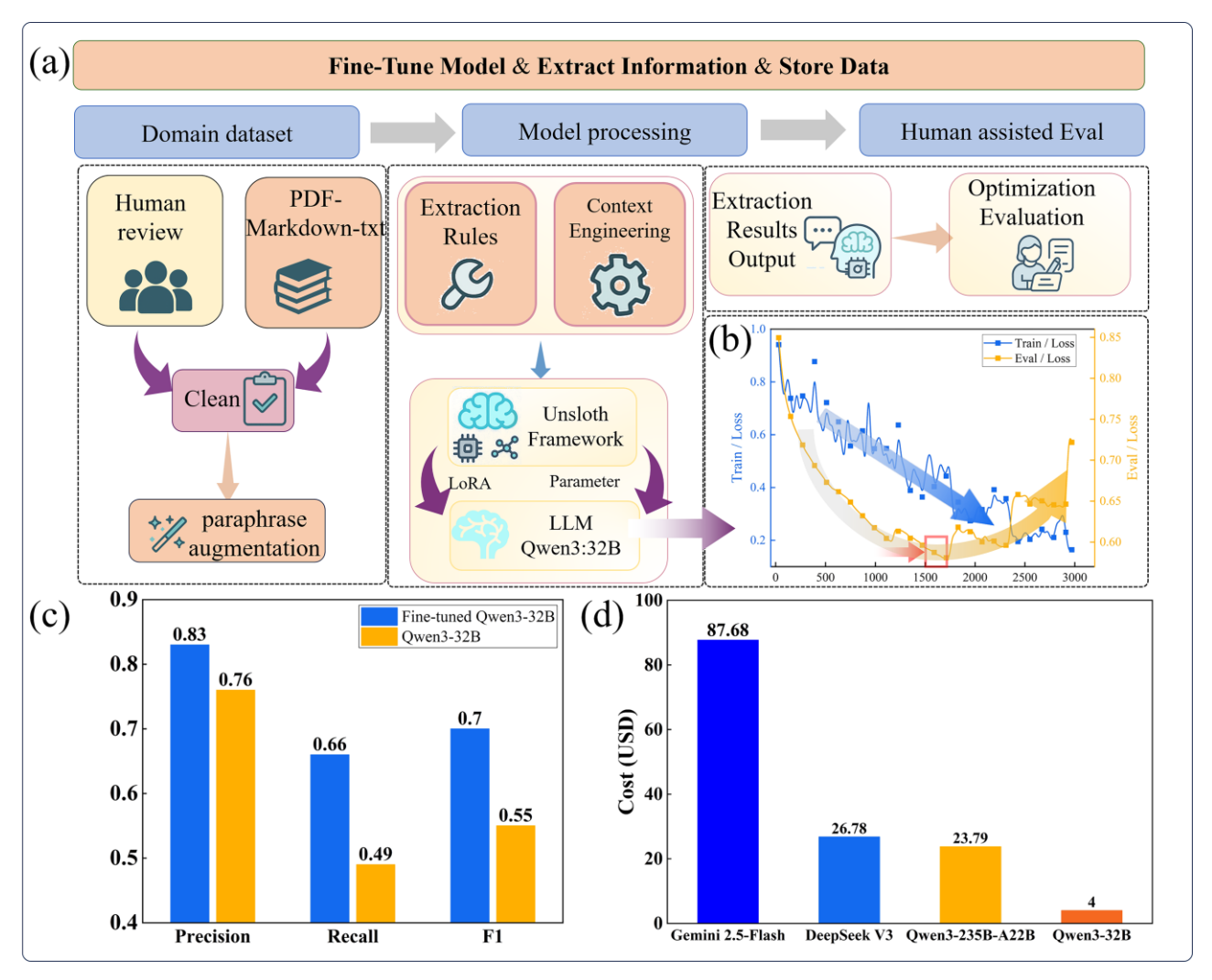


Fig. 4. (a) Schematic of the end-to-end pipeline for model fine-tuning; (b) Training and evaluation curves during fine-tuning; (c) Comparative evaluation of the fine-tuned model versus the base model (Precision, Recall, F1); (d) Cost of extracting information from 2,000 papers across different models.

2.3 Data Intelligent Management

Data management and use are as important as data extraction. To ensure long-term maintainability and reproducibility of performance and synthesis information on 2D materials, we store the extracted results in a relational database[39]. The backend uses MySQL and provides a stable, general foundation for downstream search and analysis[40]. For natural-language queries, we have built a multi-agent data intelligence system as shown in Fig. 5. When a user submits a query, the routing agent analyzes the intent and forwards the request to a SQL-generation agent to construct the statement. A safety agent reviews the SQL and blocks delete, truncate, and overwrite operations to protect the

database boundary. Approved statements are sent to an execution agent to access the database. The execution process includes retry logic and error handling. If execution fails due to syntax errors or constraint violations, the error message is fed back to the generation agent, which regenerates and validates the SQL[41]. If the failure persists, a repair agent refines the SQL statement using contextual information and error diagnostics until successful execution is achieved. A validation agent then verifies that the query results align with the original user intent. Finally, a summarization agent records the query and result for audit and decides whether to export to Excel by information granularity and use. Aggregate requests return a number, for example how many materials have a band gap greater than zero. Detailed requests provide a downloadable file, for example the records of materials with a band gap greater than zero. The system stays flexible in model choice. Each agent selects a suitable model by task difficulty to balance quality and cost. Higher-capability models are prioritized for SQL generation and repair tasks, while lightweight models handle parsing and summarization. Models can be dynamically swapped to optimize for workload and cost constraints. All agent interfaces maintain compatibility with OpenAI API conventions. For data and privacy protection, we recommend local deployment via LM Studio, Ollama, or vLLM. This supports a closed loop from question to database query, and from result checking to output packaging, without sending data outside.

2.4 Intelligent Learning for Databases

Database query quality depends on model capability. However, purely model-based methods face challenges with diverse phrasings, unclear field meanings, and complex logic—resulting in inconsistent performance and query errors. We propose a query-focused learning framework with active and passive modes. In active mode, the language model evaluates the query's importance and learning value, then automatically incorporates mappings between the query text, key fields, and validated results into the example repository. In passive mode, users retain discretion over whether to add the query mappings after execution. As examples accumulate, the system progressively deepens its understanding of tables and fields. Consequently, intent recognition accelerates, ambiguity diminishes, and both accuracy and consistency improve, while the need for repeated parsing and manual corrections decreases. This feature preserves the existing workflow while capturing reusable

knowledge from each query execution, thereby reducing token consumption and enhancing both speed and accuracy for subsequent similar queries (as illustrated in Supplementary Fig. S2). To evaluate the accuracy of materials data queries, we categorized questions into three levels of complexity: simple, medium, and complex, with 100 questions per category. Simple queries involved straightforward counting tasks, such as determining the number of instances of a specific material or the total database size. Medium-complexity queries extended these basic searches by requiring data export functionality, necessitating more sophisticated SQL workflows. Complex queries spanned multiple tables and demanded comprehensive schema knowledge, incorporating aggregation operations, fundamental calculations, and data sorting. The system achieved near-perfect accuracy (approaching 100%) on simple and medium-complexity tasks, and approximately 90% accuracy on complex tasks. This materials-focused system maintains high accuracy in data querying and extraction while significantly reducing access barriers. It delivers analysis-ready, high-quality data for synthesis pathways design, performance evaluation, and mechanistic studies, while enabling materials-centric intelligent information retrieval through intuitive human-computer interaction.

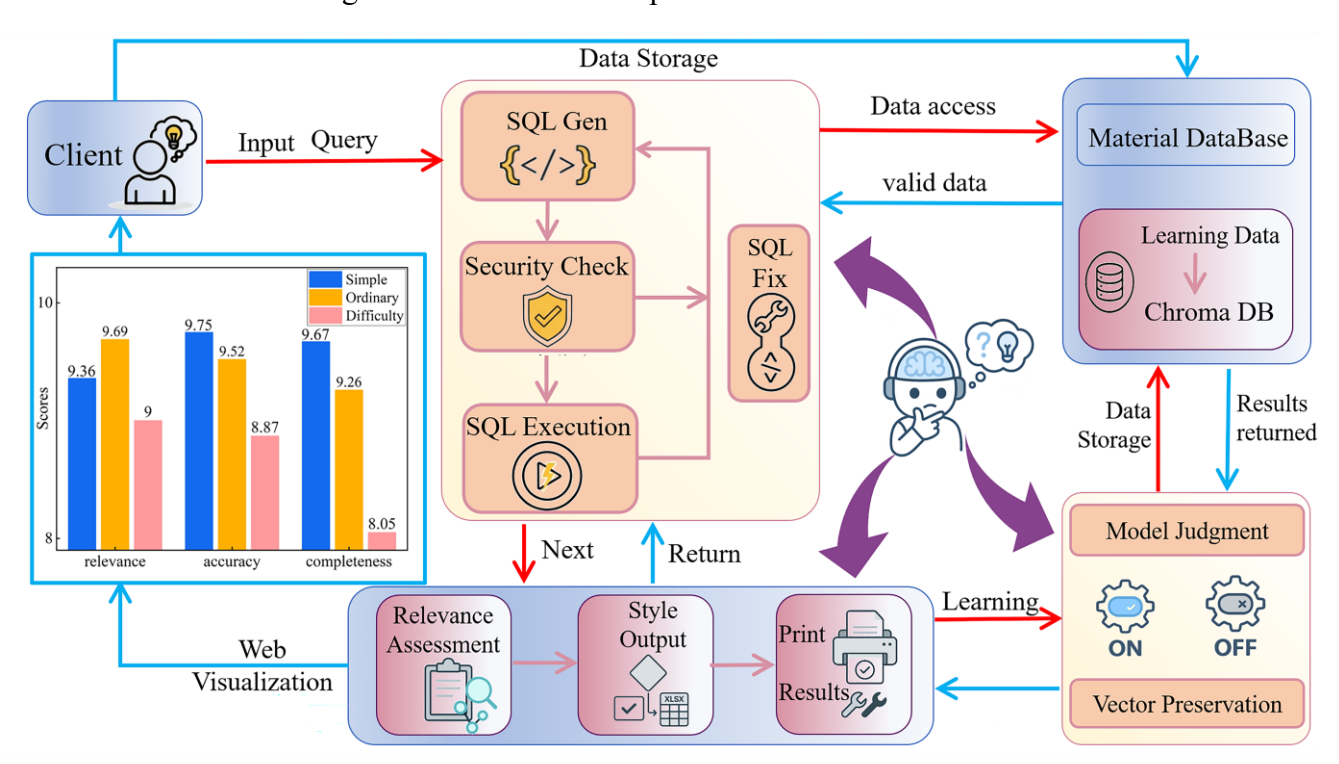


Fig. 5. Workflow for constructing the agent in the data intelligent management system, and extraction accuracy across 100 tasks at three difficulty levels—simple, ordinary, and difficult.

3. Conclusion

This work has built a structured database of 2D materials and an intelligent search and analysis platform on materials data, achieving unified standardization and traceable management of three categories of information: "structure–performance–synthesis." The results show that by combining small-sample fine-tuning for a specific domain with context engineering can significantly improve the stability and reusability of extracting 2D-materials information from the literature. Based on more than 50,000 papers, we have collected about 600,000 performance records and 202,000 synthesis records to construct a relational knowledge base, and have implemented an auditable, traceable, and secure retrieval and analysis capability via a multi-agent natural-language-to-SQL layer. Overall, this work provides a solid data foundation for optimizing synthesis pathways, conducting cross-materials-system benchmarking, and generating new hypotheses.

To further improve performance, two key aspects will be addressed in the next phase of work. First, the matching strategies in the evaluation framework will be refined to address the low recall rates caused by matching limitations, thereby more accurately reflecting the actual system performance. Second, the scope of information extraction will be expanded to encompass not only textual content but also tables and figures from the literature through systematic extraction and structured processing, enabling more comprehensive knowledge acquisition.

Declaration of competing interest

The authors declare that they have no known competing financial interests or personal relationships that could have appeared to influence the work reported in this paper.

CRediT authorship contribution statement

Lijun Shang: conducted the main research work, implemented the code, and wrote the manuscript; Yadong Yu: proposed the core research idea and provided technical guidance; Wenqiang Kang: and Dongyue Gao: assisted with manuscript writing and participated in the design of figures; Mengyan Dai: Writing –review & editing, Validation, Resources, Investigation; Pan Xiang and Zhe Liu: provided support for the code testing environment; Zhonglu Guo: conducted system testing and

provided technical guidance; **Jian Zhou** and **Zhimei Sun**: provided funding support and steer the primary research directions.

Acknowledgements

This work was supported by the National Natural Science Foundation of China (No. 52403306) and the Hebei Natural Science Foundation (No. B2024202047).

Ethical approval and consent to participate

Not applicable.

Code availability

All data and code of this study are publicly available at the GitHub repository https://github.com/Moneshanghai/database The repository includes end to end code for extracting corpora from two dimensional materials papers a data intelligence system for organization retrieval and visualization and the extracted dataset approximately six hundred thousand performance records and more than two hundred thousand synthesis records. Further inquiries can be directed to the corresponding author(s).

References

- [1] S. Hong, F. Al Marzooqi, J.K. El-Demellawi, N. Al Marzooqi, H.A. Arafat, H.N. Alshareef, ACS Materials Letters, 5 (2023) 341-356. DOI: 10.1021/acsmaterialslett.2c00914
- [2] D. Jiang, Z. Liu, Z. Xiao, Z. Qian, Y. Sun, Z. Zeng, R. Wang, J. Mater. Chem. A, 10 (2022) 89-121. DOI: 10.1039/D1TA06741A
- [3] A.J. Khan, S.S. Shah, S. Khan, A. Mateen, B. Iqbal, M. Naseem, L. He, Y. Zhang, Y. Che, Y. Tang, M. Xu, L. Gao, G. Zhao, Chem. Eng. J., 497 (2024) 154429. DOI: 10.1016/j.cej.2024.154429
- [4] P. Aghamohammadi, B. Hüner, O.C. Altıncı, E.T. Akgul, B. Teymur, U.B. Simsek, M. Demir, Int. J. Hydrogen Energy, 87 (2024) 179-198. DOI: 10.1016/j.ijhydene.2024.08.412
- [5] X. Wang, N.-D. Tran, S. Zeng, C. Hou, Y. Chen, J. Ni, npj Comput. Mater., 8 (2022) 253. DOI: 10.1038/s41524-022-00945-x
- [6] R. Ali, M. Islam, M. Shafi, S. Ali, H.-E. Wang, Coord. Chem. Rev., 540 (2025) 216797. DOI: 10.1016/j.ccr.2025.216797
- [7] S. Ogawa, S. Fukushima, M. Shimatani, Materials 2023.
- [8] Q.H. Wang, K. Kalantar-Zadeh, A. Kis, J.N. Coleman, M.S. Strano, Nat. Nanotechnol., 7 (2012) 699-712. DOI: 10.1038/nnano.2012.193
- [9] T. Xu, Y. Wang, Z. Xiong, Y. Wang, Y. Zhou, X. Li, Nano-Micro Letters, 15 (2022) 6. DOI: 10.1007/s40820-022-00976-5
- [10] H. Meskher, A.K. Thakur, S.K. Hazra, M.S. Ahamed, A.M. Saleque, Q.F. Alsalhy, M.W. Shahzad, M.N.A.S. Ivan, S. Saha, I. Lynch, Environmental Science: Nano, 12 (2025) 1012-1036. DOI: 10.1039/D4EN00427B
- [11] M.J. Statt, B.A. Rohr, D. Guevarra, S.K. Suram, T.E. Morrell, J.M. Gregoire, Scientific Data, 10 (2023) 184. DOI: 10.1038/s41597-023-02107-0
- [12] U. Celano, D. Schmidt, C. Beitia, G. Orji, A.V. Davydov, Y. Obeng, Nanoscale Advances, 6 (2024) 2260-2269. DOI: 10.1039/d3na01148h
- [13] D. Campi, N. Mounet, M. Gibertini, G. Pizzi, N. Marzari, ACS Nano, 17 (2023) 11268-11278. DOI: 10.1021/acsnano.2c11510
- [14] K. Momeni, Y. Ji, Y. Wang, S. Paul, S. Neshani, D.E. Yilmaz, Y.K. Shin, D. Zhang, J.-W. Jiang, H.S. Park, S. Sinnott, A. van Duin, V. Crespi, L.-Q. Chen, npj Comput. Mater., 6 (2020) 22. DOI: 10.1038/s41524-020-0280-2
- [15] R. Zhang, J. Zhang, Q. Chen, B. Wang, Y. Liu, Q. Qian, D. Pan, J. Xia, Y. Wang, Y. Han, Computational Materials Science, 230 (2023) 112441. DOI: 10.1016/j.commatsci.2023.112441
- [16] M. Yao, J. Ji, X. Li, Z. Zhu, J.-Y. Ge, D.J. Singh, J. Xi, J. Yang, W. Zhang, Science China Materials, 66 (2023) 2768-2776. DOI: 10.1007/s40843-022-2401-3
- [17] V. Tshitoyan, J. Dagdelen, L. Weston, A. Dunn, Z. Rong, O. Kononova, K.A. Persson, G. Ceder,
 A. Jain, Nature, 571 (2019) 95-98. DOI: 10.1038/s41586-019-1335-8
- [18] A.C. Vaucher, F. Zipoli, J. Geluykens, V.H. Nair, P. Schwaller, T. Laino, Nat. Commun., 11 (2020) 3601. DOI: 10.1038/s41467-020-17266-6
- [19] W. Wang, X. Jiang, S. Tian, P. Liu, T. Lookman, Y. Su, J. Xie, npj Comput. Mater., 9 (2023) 183. DOI: 10.1038/s41524-023-01138-w

- [20] O. Kononova, H. Huo, T. He, Z. Rong, T. Botari, W. Sun, V. Tshitoyan, G. Ceder, Scientific Data, 6 (2019) 203. DOI: 10.1038/s41597-019-0224-1
- [21] T. Gupta, M. Zaki, N.M.A. Krishnan, Mausam, npj Comput. Mater., 8 (2022) 102. DOI: 10.1038/s41524-022-00784-w
- [22] S. Lappin, Journal of Logic, Language and Information, 33 (2024) 9-20. DOI: 10.1007/s10849-023-09409-x
- [23] Z. Zheng, O. Zhang, C. Borgs, J.T. Chayes, O.M. Yaghi, J. Am. Chem. Soc., 145 (2023) 18048-18062. DOI: 10.1021/jacs.3c05819
- [24] M.P. Polak, D. Morgan, Nat. Commun., 15 (2024) 1569. DOI: 10.1038/s41467-024-45914-8
- [25] S. Yang, S. Li, S. Venugopalan, V. Tshitoyan, M. Aykol, A. Merchant, E. Cubuk, G. Cheon, arXiv (2023). DOI: 10.48550/arXiv.2311.13778
- [26] L. Schmidt, K. Hair, S. Graziosi, F. Campbell, C. Kapp, A. Khanteymoori, D. Craig, M. Engelbert, J. Thomas, arXiv, (2024). DOI: 10.48550/arXiv.2405.14445
- [27] T. Brown, B. Mann, N. Ryder, M. Subbiah, J.D. Kaplan, P. Dhariwal, A. Neelakantan, P. Shyam, G. Sastry, A. Askell, Adv. Neural Inf. Process. Syst., 33 (2020) 1877-1901. DOI: 10.48550/arXiv.2005.14165
- [28] W. Zhang, Q. Wang, X. Kong, J. Xiong, S. Ni, D. Cao, B. Niu, M. Chen, Y. Li, R. Zhang, Chemical science, 15 (2024) 10600-10611. DOI: 10.1039/d4sc00924j
- [29] M. Frohmann, I. Sterner, I. Vulić, B. Minixhofer, M. Schedl, arXiv, (2024). DOI: 10.48550/arXiv.2406.16678
- [30] L. Mei, J. Yao, Y. Ge, Y. Wang, B. Bi, Y. Cai, J. Liu, M. Li, Z.-Z. Li, D. Zhang, arXiv (2025). DOI: 10.48550/arXiv.2507.13334
- [31] J. Dagdelen, A. Dunn, S. Lee, N. Walker, A.S. Rosen, G. Ceder, K.A. Persson, A. Jain, Nat. Commun., 15 (2024) 1418. DOI: 10.1038/s41467-024-45563-x
- [32] J. Bai, S. Bai, Y. Chu, Z. Cui, K. Dang, X. Deng, Y. Fan, W. Ge, Y. Han, F. Huang, arXiv, (2023). DOI: 10.48550/arXiv.2309.16609
- [33] A. Liu, B. Feng, B. Xue, B. Wang, B. Wu, C. Lu, C. Zhao, C. Deng, C. Zhang, C. Ruan, arXiv (2024). DOI: 10.48550/arXiv.2412.19437
- [34] C. He, W. Li, Z. Jin, C. Xu, B. Wang, D. Lin, arXiv (2024). DOI: 10.48550/arXiv.2407.13773
- [35] J. Niu, Z. Liu, Z. Gu, B. Wang, L. Ouyang, Z. Zhao, T. Chu, T. He, F. Wu, Q. Zhang, arXiv (2025). DOI: 10.48550/arXiv.2509.22186
- [36] S. Garg, M. Vankadari, M. Milford, Conference on Robot Learning, PMLR2022, pp. 429-443.
- [37] E.J. Hu, Y. Shen, P. Wallis, Z. Allen-Zhu, Y. Li, S. Wang, L. Wang, W.J.I. Chen, arXiv, 1 (2022) 3. DOI: 10.48550/arXiv.2106.09685
- [38] Z. Guo, L. Xia, Y. Yu, T. Ao, C. Huang, arXiv (2024). DOI: 10.48550/arXiv.2410.05779
- [39] M.D. Wilkinson, M. Dumontier, I.J. Aalbersberg, G. Appleton, M. Axton, A. Baak, N. Blomberg, J.-W. Boiten, L.B. da Silva Santos, P.E. Bourne, Scientific data, 3 (2016) 1-9. DOI: 10.1038/sdata.2016.18
- [40] J. Zhou, L. Shen, M.D. Costa, K.A. Persson, S.P. Ong, P. Huck, Y. Lu, X. Ma, Y. Chen, H. Tang, Scientific data, 6 (2019) 86. DOI: 10.1038/s41597-019-0097-3
- [41] A. Askari, C. Poelitz, X. Tang, arXiv, 39 (2025) 23433-23441. DOI: 10.48550/arXiv.2406.12692

Supplementary Information for: LLMs-Powered Accurate Extraction, Querying and Intelligent Management of Literature-derived 2D Materials Data

Lijun Shang^{1,2}, Yadong Yu^{1,*}, Wenqiang Kang^{1,2}, Jian Zhou³, Dongyue Gao², Pan Xiang¹, Zhe Liu¹, Mengyan Dai^{1,*}, Zhonglu Guo², Zhimei Sun^{3,*}

³School of Materials Science and Engineering, and Center for Integrated Computational Materials Science, International Research Institute for Multidisciplinary Science, Beihang University, Beijing 100191, P. R. China.

*Correspondence and requests for materials should be addressed to Y. D. Yu or M. Y. Dai or Z. M. Sun: ydyu16@buaa.edu.cn, daidecai0558@163.com, zmsun@buaa.edu.cn.

¹Chemical Defense Institute, Academy of Military Sciences, Beijing 102205, China.

²Hebei Key Laboratory of Boron Nitride Micro and Nano Materials, School of Materials Science and Engineering, Hebei University of Technology, Tianjin 300130, China.

Part A — Equations

$$ratio(s,t) = \frac{2M}{|s| + |t|}$$
 (1)

Here s, t are the sequences (typically strings), |s|, |t| are their lengths, and M is the sum of the lengths of all longest, non-overlapping matching blocks between s and t. The similarity lies in [0,1] and is symmetric. We use this definition to quantify block-based sequence similarity.

$$J_2(s,t) = \frac{|G_2(s) \cap G_2(t)|}{|G_2(s) \cup G_2(t)|}, \quad G_2(s) = \{s[i]s[i+1] \mid i=1,...,|s|-1\}$$
 (2)

A string is decomposed into the set $G_2(\cdot)$ of adjacent two-character substrings, and the similarity is defined by the intersection-over-union; $|\cdot|$ denotes set cardinality and \cap , \cup are set intersection and union.

$$J_3(s,t) = \frac{|G_3(s) \cap G_3(t)|}{|G_3(s) \cup G_3(t)|}, \quad G_3(s) = \{s[i]s[i+1]s[i+2] \mid i=1,..., |s|-2\}$$
(3)

Analogously, $G_3(\cdot)$ is the set of adjacent three-character substrings; this measure emphasizes longer contiguous matches.

Part B — Figures

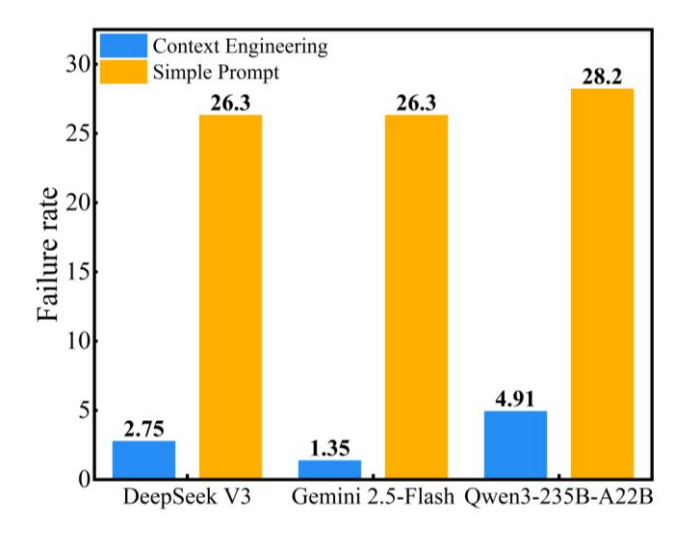


Figure S1. Failure rates for DeepSeek V3, Gemini 2.5-Flash, and Qwen3-235B-A22B under two prompting strategies. Context Engineering (blue) consistently reduces failures compared with Simple Prompt (orange) across all models.

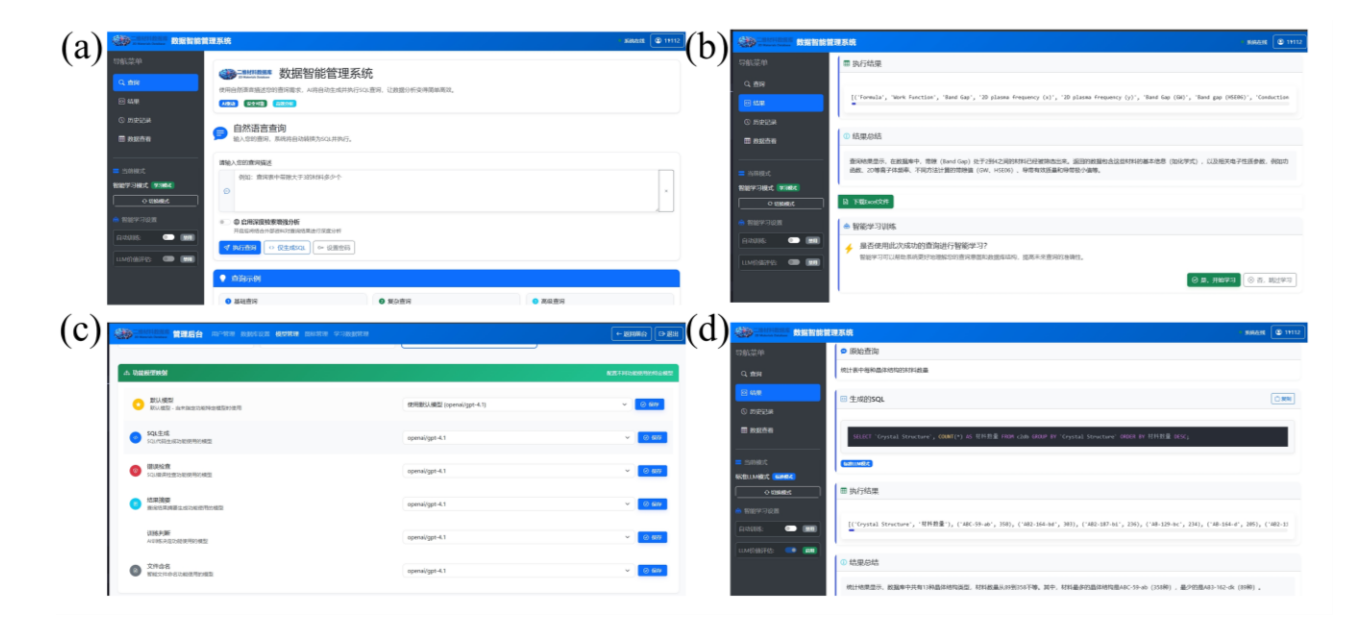


Figure S1. Overview of the data-intelligence management system and its functions:

(a) overall system interface; (b) query results in intelligent-learning mode; (c) model management interface; (d) query results in standard mode.

Part C — Tables

1. Material Performance Sample:

1	1		1
doi_or_title	material_name	parameter	value
Chem. Mater. 2022, 34, 2238–2248	PbPc	density	1.91 g/cm ³
Chem. Mater. 2022, 34, 2238-2248	lead	adsorption	-76.8 kcal/mol
	phthalocyanine	energy	
	(PbPc)		
Chem. Mater. 2022, 34, 2238–2248	lead	adsorption	-47.6 kcal/mol
	phthalocyanine	energy	
	(PbPc)		
Chem. Mater. 2022, 34, 2238-2248	lead	unit cell	$a = 52 \pm 1 \text{ Å}, b = 14 \pm 1$
	phthalocyanine	parameters	Å, $\alpha = 88 \pm 1^{\circ}$
	(PbPc)		
Chem. Mater. 2022, 34, 2238–2248	lead	unit cell	$a = b = 14 \pm 1 \text{ Å}, \alpha = 88$
	phthalocyanine	parameters	± 1°
	(PbPc)		
Chem. Mater. 2022, 34, 2238-2248	lead	gas sensitivity	NO2 sensor
	phthalocyanine		measurements

TiO2 nanoparticles-functionalized two- dimensional WO3 for highperformance supercapacitors developed by facile two-step ALD process	TiO2NP-WO3	specific capacitance improvement	1.5 times higher than pure 2D WO3 electrode
TiO2 nanoparticles-functionalized two- dimensional WO3 for highperformance supercapacitors developed by facile two-step ALD process	pure 2D WO3 electrode	specific capacitance	higher than most reported WO3 nanostructures
TiO2 nanoparticles-functionalized two- dimensional WO3 for highperformance supercapacitors developed by facile two-step ALD process	2D TiO2NP- WO3 electrode	specific capacitance	342.5, 327.1, 305.2, 290.6, and 285.3 F g-1 at current densities of 1.5, 3, 6, 15, and 30 A g-1
TiO2 nanoparticles-functionalized two- dimensional WO3 for highperformance supercapacitors developed by facile two-step ALD process	2D TiO2NP- WO3 electrode	capacitance retention	94.7% after 2000 continuous charge- discharge cycles
TiO2 nanoparticles-functionalized two- dimensional WO3 for highperformance supercapacitors developed by facile two-step ALD process	pure 2D WO3 electrode	specific capacitance	226.1, 208.5, 197.9, 194.6, and 190.3 F g-1 at current densities of 1.5, 3, 6, 15, and 30 A g-1
TiO2 nanoparticles-functionalized two- dimensional WO3 for highperformance supercapacitors developed by facile two-step ALD process	pure 2D WO3 electrode	capacitance retention	92.5% after 2000 continuous charge- discharge cycles
TiO2 nanoparticles-functionalized two- dimensional WO3 for highperformance supercapacitors developed by facile two-step ALD process	2D WO3	voltage range	0-0.8 V
TiO2 nanoparticles-functionalized two- dimensional WO3 for highperformance supercapacitors developed by facile two-step ALD process	2D WO3	scan rate	1–50 mV s–1
TiO2 nanoparticles-functionalized two- dimensional WO3 for highperformance supercapacitors developed by facile two-step ALD process	2D WO3	current density	1.5–30 A g–1
TiO2 nanoparticles-functionalized two- dimensional WO3 for highperformance supercapacitors developed by facile two-step ALD process	2D WO3	cycling stability	measured at 6 A g-1 over 2000 cycles
TiO2 nanoparticles-functionalized two- dimensional WO3 for highperformance	2D WO3	thickness	$5.905 \pm 0.325 \text{ nm}$

supercapacitors developed by facile			
two-step ALD process			
TiO2 nanoparticles-functionalized two-	2D TiO2NP-	voltage range	0-0.8 V
dimensional WO3 for highperformance	WO3		
supercapacitors developed by facile	-		
two-step ALD process			
TiO2 nanoparticles-functionalized two-	2D TiO2NP-	scan rate	1-50 mV s-1
dimensional WO3 for highperformance	WO3		
supercapacitors developed by facile			
two-step ALD process			
TiO2 nanoparticles-functionalized two-	2D TiO2NP-	current density	1.5-30 A g-1
dimensional WO3 for highperformance	WO3	•	S
supercapacitors developed by facile			
two-step ALD process			
TiO2 nanoparticles-functionalized two-	2D TiO2NP-	molar amount	10.76 mol%
dimensional WO3 for highperformance	WO3	of TiO2	
supercapacitors developed by facile			
two-step ALD process			
TiO2 nanoparticles-functionalized two-	2D TiO2NP-	thickness	$1.587 \pm 0.013 \text{ nm}$
dimensional WO3 for highperformance	WO3		
supercapacitors developed by facile			
two-step ALD process			
TiO2 nanoparticles-functionalized two-	2D TiO2	thickness	$1.587 \pm 0.013 \text{ nm}$
dimensional WO3 for highperformance			
supercapacitors developed by facile			
two-step ALD process			
TiO2 nanoparticles-functionalized two-	2D TiO2	average growth	0.71015 Å per cycle
dimensional WO3 for highperformance		rate	
supercapacitors developed by facile			
two-step ALD process			
TiO2 nanoparticles-functionalized two-	2D TiO2	number of ALD	20
dimensional WO3 for highperformance		cycles	
supercapacitors developed by facile			
two-step ALD process			
Photonic enhanced flexible	PFM-100 film	Seebeck	19.43 $\mu V/K$
photothermoelectric generator using		coefficient	
MXene coated fullerenes	DTD 6 106 71		210 11
Photonic enhanced flexible	PFM-100 film	Output voltage	210 μV
photothermoelectric generator using			
MXene coated fullerenes			1.00 - 77
Photonic enhanced flexible	PFM-100 film	Output voltage	169 μV
photothermoelectric generator using			
MXene coated fullerenes			

Photonic enhanced flexible	PFM-100 film	Output voltage	317 μV
photothermoelectric generator using			
MXene coated fullerenes			
Photonic enhanced flexible	PFM-100 film	Output voltage	349 μV
photothermoelectric generator using			
MXene coated fullerenes			
Photonic enhanced flexible	PFM-100 film	PT output	2.02 mV
photothermoelectric generator using		voltage	
MXene coated fullerenes			
Photonic enhanced flexible	PFM-100 film	PT output	1.44 mV
photothermoelectric generator using		voltage	
MXene coated fullerenes			
Photonic enhanced flexible	PFM-100 film	Output voltage	1.04 mV
photothermoelectric generator using			
MXene coated fullerenes			
Photonic enhanced flexible	PFM-100 film	Output voltage	1.59 mV
photothermoelectric generator using		-	
MXene coated fullerenes			
Photonic enhanced flexible	PFM-100 film	Output voltage	2.15 mV
photothermoelectric generator using		-	
MXene coated fullerenes			
Photonic enhanced flexible	PFM-100 film	Output voltage	1.8 mV
photothermoelectric generator using			
MXene coated fullerenes			
Photonic enhanced flexible	PFM-100 film	VTE	165.29 μV
photothermoelectric generator using			
MXene coated fullerenes			
Photonic enhanced flexible	PFM-100 film	VTE	197.29 μV
photothermoelectric generator using			
MXene coated fullerenes			
Photonic enhanced flexible	PFM-100	Seebeck	18.13 μV/K
photothermoelectric generator using		coefficient	
MXene coated fullerenes			
Photonic enhanced flexible	PFM-100	output voltage	1.04 mV
photothermoelectric generator using		at 15 mW	
MXene coated fullerenes			
Photonic enhanced flexible	PFM-100	output voltage	1.59 mV
photothermoelectric generator using		at 20 mW	
MXene coated fullerenes			
Photonic enhanced flexible	PFM-100	output voltage	2.15 mV
photothermoelectric generator using		at 25 mW	
MXene coated fullerenes			

Photonic enhanced flexible	PFM-150	Seebeck	19.57 μV/Κ
photothermoelectric generator using		coefficient	
MXene coated fullerenes			
Direct evidence of a charge depletion	FeSe	distance from	0.43 nm
region at the interface of Van der Waals	monolayer	STO surface	
monolayers and dielectric oxides: The	•		
case of superconducting FeSe/STO			
Direct evidence of a charge depletion	FeSe	depletion layer	$6.5 \pm 1 \text{ nm}$
region at the interface of Van der Waals	monolayer	thickness	
monolayers and dielectric oxides: The			
case of superconducting FeSe/STO			
Direct evidence of a charge depletion	FeSe ML	superconducting	$11 \pm 3 \text{ meV}$
region at the interface of Van der Waals		gap	
monolayers and dielectric oxides: The			
case of superconducting FeSe/STO			
Direct evidence of a charge depletion	Nb-STO	plasma	83 meV
region at the interface of Van der Waals		frequency	
monolayers and dielectric oxides: The			
case of superconducting FeSe/STO			
Direct evidence of a charge depletion	Nb-STO	carrier	1.18×10^26 m ⁻³
region at the interface of Van der Waals		concentration	
monolayers and dielectric oxides: The			
case of superconducting FeSe/STO			
Direct evidence of a charge depletion	FeSe	plasma	334 meV
region at the interface of Van der Waals		frequency	
monolayers and dielectric oxides: The			
case of superconducting FeSe/STO			
Direct evidence of a charge depletion	FeSe	effective mass	3
region at the interface of Van der Waals			
monolayers and dielectric oxides: The			
case of superconducting FeSe/STO			
Direct evidence of a charge depletion	FeSe	carrier density	0.12 e ⁻ /Fe
region at the interface of Van der Waals			
monolayers and dielectric oxides: The			
case of superconducting FeSe/STO			
Direct evidence of a charge depletion	Nb-STO	plasma	83 meV
region at the interface of Van der Waals		frequency	
monolayers and dielectric oxides: The			
case of superconducting FeSe/STO			
Direct evidence of a charge depletion	Nb-STO	plasmon	75 meV
region at the interface of Van der Waals		linewidth (γpl)	
monolayers and dielectric oxides: The			
case of superconducting FeSe/STO			

Direct evidence of a charge depletion	Nb-STO	plasmon	5 meV
region at the interface of Van der Waals		linewidth (γ0)	
monolayers and dielectric oxides: The			
case of superconducting FeSe/STO			
Direct evidence of a charge depletion	STO	background	5.9
region at the interface of Van der Waals		dielectric	
monolayers and dielectric oxides: The		constant	
case of superconducting FeSe/STO			
Prediction of synthesis of ternary-	Mo2TiAlC2	relative	-0.082 eV
layered double transition metal MAX		formation	
phases and the possibility of their		energy (ΔH)	
exfoliation for formation of 2D MXenes		 , ,	
Prediction of synthesis of ternary-	Cr2TiAlC2	relative	-0.031 eV
layered double transition metal MAX		formation	
phases and the possibility of their		energy (ΔH)	
exfoliation for formation of 2D MXenes			
Prediction of synthesis of ternary-	Mo2ScAlC2	relative	-0.037 eV
layered double transition metal MAX		formation	
phases and the possibility of their		energy (ΔH)	
exfoliation for formation of 2D MXenes			
Prediction of synthesis of ternary-	Mo2ScAlC2	exfoliation	0.202 eV/Ų
layered double transition metal MAX		energy (Eexf)	
phases and the possibility of their			
exfoliation for formation of 2D MXenes			
Prediction of synthesis of ternary-	Mo2TiAlC2	exfoliation	0.201 eV/Å ²
layered double transition metal MAX		energy (Eexf)	
phases and the possibility of their			
exfoliation for formation of 2D MXenes			
Prediction of synthesis of ternary-	Cr2TiAlC2	exfoliation	$0.206~\mathrm{eV/Å^2}$
layered double transition metal MAX		energy (Eexf)	
phases and the possibility of their			
exfoliation for formation of 2D MXenes			
Optical properties of thin layers of	ReSe2	in-plane force	$18.9\times10^{\wedge}19~N/m^3$
rhenium diselenide (ReSe2) with		constant (Ks)	
thickness ranging from mono- (1 ML) to			
nona-layer (9 MLs) are demonstrated.			
Optical properties of thin layers of	ReSe2	out-of-plane	$69.6 \times 10^{19} \text{ N/m}^3$
rhenium diselenide (ReSe2) with		force constant	
thickness ranging from mono- (1 ML) to		(Kb)	
nona-layer (9 MLs) are demonstrated.			
Optical properties of thin layers of	ReSe2	blueshift of	about 120 meV
rhenium diselenide (ReSe2) with		emission lines	
thickness ranging from mono- (1 ML) to			
nona-layer (9 MLs) are demonstrated.			

Optical properties of thin layers of	ReSe2	energy	about 55 meV for
rhenium diselenide (ReSe2) with		separation	monolayer to almost 20
thickness ranging from mono- (1 ML) to		between X1 and	meV for 9 MLs
nona-layer (9 MLs) are demonstrated.		X2 peaks	
Optical properties of thin layers of	ReSe2	emission energy	about 1.51 eV for 1 ML
rhenium diselenide (ReSe2) with		for X1 peak	to ~1.39 eV for 9 MLs
thickness ranging from mono- (1 ML) to		•	
nona-layer (9 MLs) are demonstrated.			
Optical properties of thin layers of	ReSe2	energy	around 12 cm-1 for 1
rhenium diselenide (ReSe2) with		difference	ML to almost 6 cm-1 in
thickness ranging from mono- (1 ML) to		between two	7-9 MLs
nona-layer (9 MLs) are demonstrated.		phonon modes	
Optical properties of thin layers of	ReSe2	energy	12 cm-1 to almost 6
rhenium diselenide (ReSe2) with		difference	cm-1
thickness ranging from mono- (1 ML) to		between peaks 1	
nona-layer (9 MLs) are demonstrated.		and 2	
Optical properties of thin layers of	ReSe2	blueshift of	about 120 meV
rhenium diselenide (ReSe2) with		phonon mode	
thickness ranging from mono- (1 ML) to		-	
nona-layer (9 MLs) are demonstrated.			
Optical properties of thin layers of	ReSe2	blueshift of	almost 4 cm-1
rhenium diselenide (ReSe2) with		phonon mode	
thickness ranging from mono- (1 ML) to			
nona-layer (9 MLs) are demonstrated.			
Optical properties of thin layers of	ReSe2	energy	almost 12 cm-1 for a
rhenium diselenide (ReSe2) with		difference	monolayer
thickness ranging from mono- (1 ML) to		between peaks 1	
nona-layer (9 MLs) are demonstrated.		and 2	
Room temperature synthesis of	Mn3O4	specific	537 F/g (at 2 A g-1)
freestanding 2D Mn3O4 nanostructures		capacitance	
with enriched electrochemical properties			
for supercapacitor application			
Room temperature synthesis of	Mn3O4	specific	93% (up to 5000 cycles)
freestanding 2D Mn3O4 nanostructures		capacitance	
with enriched electrochemical properties		retention	
for supercapacitor application			
Room temperature synthesis of	2D Mn3O4	specific	537 F/g at 2 A g-1
freestanding 2D Mn3O4 nanostructures	nanoplatelets	capacitance	
with enriched electrochemical properties			
for supercapacitor application			
Room temperature synthesis of	2D Mn3O4	cyclic stability	93% retention up to 5000
freestanding 2D Mn3O4 nanostructures	nanoplatelets		cycles
with enriched electrochemical properties			
for supercapacitor application			

Room temperature synthesis of	2D Mn3O4	specific	236 F/g at 5 mV/s scan
freestanding 2D Mn3O4 nanostructures	nanoplatelets	capacitance	rate
with enriched electrochemical properties	1	1	
for supercapacitor application			
Room temperature synthesis of	2D Mn3O4	equivalent	5.28 Ohm
freestanding 2D Mn3O4 nanostructures	nanoplatelets	series resistance	
with enriched electrochemical properties	1	(Rs)	
for supercapacitor application		()	
Room temperature synthesis of	2D Mn3O4	charge transfer	14.41 Ohm
freestanding 2D Mn3O4 nanostructures	nanoplatelets	resistance (Rct)	
with enriched electrochemical properties		10010100100 (1100)	
for supercapacitor application			
Room temperature synthesis of	2D Mn3O4	Warburg	45.7 Ohm
freestanding 2D Mn3O4 nanostructures	nanoplatelets	impedance	13.7 01111
with enriched electrochemical properties	initiopiutetets	(W1)	
for supercapacitor application		("' 1)	
Room temperature synthesis of	2D Mn3O4	specific	537 F/g
freestanding 2D Mn3O4 nanostructures	nanoplatelets	capacitance	20,116
with enriched electrochemical properties	папоріанствия	capacitance	
for supercapacitor application			
Room temperature synthesis of	2D Mn3O4	specific	219 F/g
freestanding 2D Mn3O4 nanostructures	nanoplatelets	capacitance	217176
with enriched electrochemical properties	nanopiateiets	сарастанес	
for supercapacitor application			
Room temperature synthesis of	2D Mn3O4	specific	137 F/g
freestanding 2D Mn3O4 nanostructures	nanoplatelets	capacitance	137 17g
with enriched electrochemical properties	nanopiateiets	сарастанес	
for supercapacitor application			
Room temperature synthesis of	2D Mn3O4	specific surface	39.06 m2/g
freestanding 2D Mn3O4 nanostructures	nanoplatelets	•	39.00 m2/g
with enriched electrochemical properties	nanopiateiets	area	
for supercapacitor application			
	2D Mn2O4	0.1.040.000.40.040	2.76
Room temperature synthesis of	2D Mn3O4	average pore	2.76 nm
freestanding 2D Mn3O4 nanostructures	nanoplatelets	width	
with enriched electrochemical properties			
for supercapacitor application	2D M.: 204		24.25
Room temperature synthesis of	2D Mn3O4	crystallite size	24.25 nm
freestanding 2D Mn3O4 nanostructures	nanoplatelets		
with enriched electrochemical properties			
for supercapacitor application	an 14 and		
Room temperature synthesis of	2D Mn3O4	thickness	3.5 nm
freestanding 2D Mn3O4 nanostructures	nanoplatelets		
with enriched electrochemical properties			
for supercapacitor application			

Room temperature synthesis of freestanding 2D Mn3O4 nanostructures with enriched electrochemical properties	2D Mn3O4 nanoplatelets	thickness	5.1 nm
for supercapacitor application			
Room temperature synthesis of	2D Mn3O4	length	100–200 nm
freestanding 2D Mn3O4 nanostructures	nanoplatelets		
with enriched electrochemical properties			
for supercapacitor application			
Room temperature synthesis of	2D Mn3O4	width	40–60 nm
freestanding 2D Mn3O4 nanostructures	nanoplatelets		
with enriched electrochemical properties			
for supercapacitor application			
Progress in the materials science of	silicene	band gap at	1.55 meV
silicene		Dirac points	
		(buckled	
		silicene)	
Progress in the materials science of	silicene	band gap at	2.90 meV
silicene		Dirac points	
		(buckled	
		silicene with in-	
		plane stress)	
Progress in the materials science of	silicene	band gap at	0.07 meV
silicene		Dirac points	
		(planar silicene)	
Progress in the materials science of	silicene	Si-Si bond	2.24 Å
silicene		length in	
		epitaxial	
		silicene	
Progress in the materials science of	silicene	Si-Si bond	2.35 Å
silicene		length in bulk	
		diamond-	
		structured	
		silicon	
Progress in the materials science of	silicene	Si-Si bond	2.14–2.16 Å
silicene		length in	
		disilenes	
Progress in the materials science of	silicene	in-plane lattice	3.855 Å
silicene		constant of	
		freestanding	
		silicene	
Progress in the materials science of	•••	:1	3.84 Å
riogress in the materials science of	silicene	in-plane lattice	3.04 A
silicene	silicene	constant of	3.04 A

Progress in the materials science of silicene	silicene	band gap in epitaxial silicene nanoribbons	0.5 eV						
Progress in the materials science of silicene	silicene energy of π bands in epitaxial silicene nanoribbons		bands in epitaxial silicene		silicene energy of π bands in epitaxial silicene		silicene energy of π bands in epitaxial silicene		0.6 eV below the Fermi level
Progress in the materials science of silicene	silicene	width of epitaxial silicene nanoribbons	1.6 nm						
Progress in the materials science of silicene	silicene	height of epitaxial silicene nanoribbons	0.2 nm						
Progress in the materials science of silicene	silicene on ZrB2(0001)	thermal stability	above 650 °C						
Progress in the materials science of silicene	silicene on ZrC(111)	thermal stability	about 730 °C						
Progress in the materials science of silicene	ZrB2(0001)	surface coverage with silicene	more than 99.5%						
Progress in the materials science of silicene	ZrB2(0001)	lattice constant	about 3.65 Å						
Progress in the materials science of silicene	ZrB2(0001)	compression relative to bulk Si(111) bilayer	5%						
Progress in the materials science of silicene	ZrB2(0001)	binding energy of Si 2p3/2 doublet	600 ± 5 meV (spin–orbit splitting)						
Progress in the materials science of silicene	ZrB2(0001)	binding energy shift of silicene 2p3/2 line	450–710 meV towards lower binding energy						
Progress in the materials science of silicene	ZrB2(0001)	energy gap observed by scanning tunneling spectroscopy	350 meV, with center shifted 60 meV below the Fermi level						

2. Synthesis Methods Sample

doi_or_title	material_	method_na	method_detail	reagents	conditions	equipment
	name	me	S			

Two dimensional (2D) materials such as graphene and transition metal dichalcogenides (TMDs) are promising for optical modulation, detection, and light emission since their material properties can be tuned on-demand via	WS2	Large-area synthesis	Large-area synthesis of high-quality and uniform monolayer WS2 on reusable Au foils.	Au foils	Not specified in the text	Not specified in the text
electrostatic doping Two dimensional (2D) materials such as graphene and transition metal dichalcogenides (TMDs) are promising for optical modulation, detection, and light emission since their material properties can be tuned on-demand via electrostatic doping	WS2	Synthesis of Large-Area WS2 monolayers	Synthesis of Large-Area WS2 monolayers with Exceptional Photolumines cence.	Not specified in the text	Not specified in the text	Not specified in the text
Two dimensional (2D) materials such as graphene and transition metal dichalcogenides (TMDs) are promising for optical modulation, detection, and light emission since their material properties can be tuned on-demand via electrostatic doping	MoS2	Synthesis of MoS2	Synthesis of MoS2 film for capacitive device experiments.	Not specified in the text	Not specified in the text	Not specified in the text
Two dimensional (2D) materials such as graphene and transition metal dichalcogenides (TMDs) are promising for optical modulation, detection, and light emission since their material properties can be tuned on-demand via electrostatic doping	monolay er WS2	metal- organic chemical vapor deposition (MOCVD)	A 30 µm arc length of WS2 is grown using metalorganic chemical vapor deposition (MOCVD) and then patterned	WS2 (tungsten disulphide), ionic liquid [P14][FAP], Ti/Au contacts	Applied voltage of 2 V, room temperatur e, atmospher ic exposure	Microring resonator, Ti/Au electrodes, ionic liquid [P14][FAP] , COMSOL Multiphysic s simulations

			onto the ring.			
			The			
			monolayer			
			WS2 is			
			electrically			
			contacted			
			with Ti/Au			
			electrodes for			
			gating. The			
			ionic liquid			
			[P14][FAP] is			
			used for			
			electrostatic			
			doping, where			
			a potential			
			difference is			
			applied			
			between the			
			electrode			
			connected to			
			WS2 and a			
			nearby			
			counter			
			electrode,			
			resulting in			
			ion			
			accumulation			
			at the surface			
			of WS2. The			
			maximum			
			electron			
			doping			
			density			
			induced in the			
			monolayer is			
			about 7.2 \pm			
			0.8 x 10^13			
			cm^-2 with			
			an applied			
			voltage of 2			
			V.			
Two dimensional (2D)	monolay	chemical	CVD-grown	WS2	Voltage	MZI (Mach
materials such as	er WS2	vapor	films of WS2	(tungsten	swing in	Zehnder
graphene and transition		_	are used for	disulphide),	the range	interferome
				- //		

metal dichalcogenides	deposition	capacitive	HfO2	of -8 V to	ter), HfO2-
(TMDs) are promising	(CVD)	devices.	(hafnia),	9 V, room	ITO
for optical modulation,	(CVD)	These films	ITO	temperatur	capacitor,
detection, and light		are patterned	(indium tin	e	SU-8
emission since their		on both arms	oxide)	C	photoresist
material properties can		of the MZI,	oxide)		for high
be tuned on-demand via		followed by			index
electrostatic doping		the deposition			cladding,
electrostatic doping		of metal			COMSOL
		electrodes.			Multiphysic
		The ionic			S
		liquid			simulations
		[P14][FAP] is			Simulations
		replaced with			
		a stack of			
		HfO2 (hafnia)			
		and			
		transparent			
		conducting			
		oxide ITO			
		(indium tin			
		oxide) to			
		form the			
		TMD-HfO2-			
		ITO capacitor			
		on the SiN			
		waveguide.			
		The charge			
		neutrality			
		point for the			
		monolayer			
		WS2 is at -4			
		V,			
		corresponding			
		to an initial			
		electron			
		doping of 1.5			
		$\pm~0.2\times10^{\wedge}12$			
		cm^-2, likely			
		due to sulfur			
		vacancies			
		from CVD			
		growth.			

Two dimensional (2D)	WS2-	capacitive	The WS2-	WS2	Voltage	MZI (Mach
materials such as	HfO2-	configuratio	HfO2-ITO	(tungsten	swing in	Zehnder
graphene and transition	ITO	n	capacitor is	disulphide),	the range	interferome
metal dichalcogenides	capacitor		fabricated on	HfO2	of -8 V to	ter), HfO2-
(TMDs) are promising	1		each arm of	(hafnia),	9 V, room	ITO
for optical modulation,			the MZI. The	ITO	temperatur	capacitor,
detection, and light			monolayer	(indium tin	e	SU-8
emission since their			WS2 is	oxide)		photoresist
material properties can			patterned on			for high
be tuned on-demand via			both arms of			index
electrostatic doping			the MZI,			cladding,
			followed by			COMSOL
			the deposition			Multiphysic
			of metal			S
			electrodes.			simulations
			The ionic			
			liquid			
			[P14][FAP] is			
			replaced with			
			a stack of			
			HfO2 (hafnia)			
			and			
			transparent			
			conducting			
			oxide ITO			
			(indium tin			
			oxide) to			
			form the			
			TMD-HfO2-			
			ITO capacitor on the SiN			
			waveguide.			
			The charge			
			neutrality			
			point for the			
			monolayer			
			WS2 is at -4			
			V,			
			corresponding			
			to an initial			
			electron			
			doping of 1.5			
			± 0.2 × 10^12			
			cm^-2, likely			

			due to sulfur vacancies from CVD growth.			
Rational and green synthesis of novel two-dimensional WS2/MoS2 heterojunction via direct exfoliation in ethanol-water targeting advanced visible-light-responsive photocatalytic performance	few-layer WS2	Direct exfoliation in ethanol- water mixed solution	Commercial WS2 powders were dispersed in ethanol-water mixed solution to form a suspension with an initial concentration of 8 mg/mL. The suspension was then sonicated at 150 W for 8 h. After sonication, the dispersion underwent centrifugation at 3344 rpm for 30 min, and the supernatants containing few-layered WS2 were collected for further use.	WS2 powders, ethanol- water mixed solution	Sonication at 150 W for 8 h, centrifugat ion at 3344 rpm for 30 min	Ultrasonic bath, centrifuge
Rational and green synthesis of novel two- dimensional WS2/MoS2 heterojunction via direct exfoliation in ethanol- water targeting advanced visible-light-responsive photocatalytic performance	WS2/Mo S2 heterostr ucture	In-situ hydrotherm al reaction	Ammonium molybdate tetrahydrate (H32Mo7N6 O28, 0.6 g) and thiourea (CN2H4S, 4.8 g) were dissolved	Ammonium molybdate tetrahydrate (0.6 g), thiourea (4.8 g), WS2 nanosheet suspension	Hydrother mal reaction at 200 °C for 24 h, vacuum drying at 60 °C overnight	Teflon- lined stainless- steel autoclave, vacuum oven, filtration system

			uniformly in			
			60 mL of			
			WS2			
			nanosheet			
			suspension			
			(prepared in			
			ethanol-water			
			mixed			
			solution) and			
			stirred for 60			
			min. The			
			mixture was			
			sonicated for			
			another 30			
			min at 28			
			kHz. It was			
			then			
			transferred			
			into a Teflon-			
			lined			
			stainless-steel			
			autoclave and			
			reacted at			
			200 °C for 24			
			h. After			
			cooling to			
			room			
			temperature,			
			the black			
			precipitates			
			were			
			collected by			
			filtration,			
			washed with			
			DI water and			
			ethanol, and			
			dried in a			
			vacuum oven			
			at 60 °C			
Rational and green	WS2	Liquid	overnight. The starting	WS2	Ethanol/w	Ultrasonic
synthesis of novel two-	nanoshee	exfoliation	material is	w 52 powder	ater	bath,
dimensional WS2/MoS2		(LPE)	commercializ	(Aladdin-	volume	centrifuge,
heterojunction via direct	ts	(LIL)	ed WS2		ratio of	UV-vis
neterojunetion via unect			cu wsz	reagent	14110 01	O v -v18
			18			

exfoliation in ethanol-	powder	Inc.),	7/3 (v/v),	spectromete
water targeting advanced	(Aladdin-	ethanol,	sonication,	r,
visible-light-responsive	reagent Inc.).	water	centrifugat	photolumin
photocatalytic	The powders		ion	escence
performance	are added into			(PL)
•	an ethanol-			spectromete
	water mixture			r, SEM,
	and subjected			TEM,
	to sonication			AFM,
	and			Raman
	centrifugation			spectromete
	to form WS2			r
	suspensions.			
	By varying			
	the volume			
	ratio of			
	ethanol and			
	water, a series			
	of			
	suspensions			
	containing			
	uniformly-			
	distributed			
	WS2			
	nanosheets			
	can be			
	attained. The			
	optimal			
	condition is			
	found to be			
	an			
	ethanol/water			
	volume ratio			
	of 7/3, which			
	leads to the			
	highest concentration			
	of exfoliated			
	WS2 (0.2 mg			
	mL-1) and a			
	dark greenish colour. This			
	mild and			
	green			

			exfoliation process			
			produces			
			uniform and			
			stable WS2			
			inks without			
			further			
-			purification.			
Rational and green	WS2/Mo	Hydrotherm	WS2/MoS2	Ammonium	Hydrother	Hydrother
synthesis of novel two-	S2	al synthesis	heterojunctio	molybdate	mal	mal reactor,
dimensional WS2/MoS2	heterojun		ns are	tetrahydrate	reaction,	SEM,
heterojunction via direct	ctions		prepared	(H32Mo7N	volume	TEM, EDS,
exfoliation in ethanol-			using a	6O28, 0.6	ratios of	XRD, XPS
water targeting advanced			hydrothermal	g), thiourea	WS2	
visible-light-responsive			route. LPE-	(CN2H4S,	suspensio	
photocatalytic			derived WS2	4.8 g), WS2	n/water	
performance			nanosheets	nanosheet	(S/W):	
			serve as 2D	suspensions	3/7, 1/1,	
			growth		7/3, and	
			substrates.		4/1	
			Ammonium			
			molybdate			
			tetrahydrate			
			(H32Mo7N6			
			O28, 0.6 g)			
			and thiourea			
			(CN2H4S,			
			4.8 g) are			
			dissolved uniformly in			
			60 mL of			
			WS2			
			nanosheet			
			suspensions.			
			The mixture			
			undergoes a			
			hydrothermal			
			reaction to			
			produce			
			WS2/MoS2			
			heterojunctio			
			ns via self-			
			assembly.			
			Different			

			concentration			
			s of WS2			
			suspensions			
			are attempted			
			(volume			
			ratios of WS2			
			suspension/w			
			ater: 3/7, 1/1,			
			7/3, and $4/1$).			
			The optimal			
			condition is			
			found to be			
			an			
			ethanol/water			
			volume ratio			
			of 7/3, which			
			leads to the			
			formation of			
			blossoming			
			flower-like			
			structures			
			instead of			
			tightly-			
			aggregated			
			spheres due to			
			the 2D WS2			
			the 2D WS2 template			
Protected giant magnetic	WS2	Defect-	template	TM atoms	Low	Not
	WS2	Defect- induced	template effect.	TM atoms (transition	Low temperatur	Not specified
nisotropy in two-	WS2		template effect. The synthesis			
nnisotropy in two- limensional materials:	WS2	induced	template effect. The synthesis involves the	(transition	temperatur	
nnisotropy in two- dimensional materials: Fransition-metal adatoms	WS2	induced	template effect. The synthesis involves the creation of	(transition metals),	temperatur e, low	
nnisotropy in two- dimensional materials: Fransition-metal adatoms on defected tungsten	WS2	induced	template effect. The synthesis involves the creation of sulfur vacancies	(transition metals), WS2	temperatur e, low concentrat ion of TM	
nnisotropy in two- limensional materials: Fransition-metal adatoms on defected tungsten	WS2	induced	template effect. The synthesis involves the creation of sulfur	(transition metals), WS2 monolayer	temperatur e, low concentrat	
nisotropy in two- limensional materials: Fransition-metal adatoms on defected tungsten	WS2	induced	template effect. The synthesis involves the creation of sulfur vacancies (Vs) in WS2	(transition metals), WS2 monolayer with sulfur vacancies	temperatur e, low concentrat ion of TM atoms,	
nnisotropy in two- limensional materials: Fransition-metal adatoms on defected tungsten	WS2	induced	template effect. The synthesis involves the creation of sulfur vacancies (Vs) in WS2 monolayers.	(transition metals), WS2 monolayer with sulfur	temperatur e, low concentrat ion of TM atoms, presence	
anisotropy in two- dimensional materials: Γransition-metal adatoms on defected tungsten	WS2	induced	template effect. The synthesis involves the creation of sulfur vacancies (Vs) in WS2 monolayers. These Vs can be either	(transition metals), WS2 monolayer with sulfur vacancies (Vs), H2S,	temperatur e, low concentrat ion of TM atoms, presence of sulfur vacancies	
anisotropy in two- dimensional materials: Transition-metal adatoms on defected tungsten	WS2	induced	template effect. The synthesis involves the creation of sulfur vacancies (Vs) in WS2 monolayers. These Vs can	(transition metals), WS2 monolayer with sulfur vacancies (Vs), H2S, S6, S8 (as	temperatur e, low concentrat ion of TM atoms, presence of sulfur	
Protected giant magnetic anisotropy in two-dimensional materials: Transition-metal adatoms on defected tungsten disulfide monolayer	WS2	induced	template effect. The synthesis involves the creation of sulfur vacancies (Vs) in WS2 monolayers. These Vs can be either naturally formed	(transition metals), WS2 monolayer with sulfur vacancies (Vs), H2S, S6, S8 (as common sulfur	temperatur e, low concentrat ion of TM atoms, presence of sulfur vacancies	
anisotropy in two- dimensional materials: Transition-metal adatoms on defected tungsten	WS2	induced	template effect. The synthesis involves the creation of sulfur vacancies (Vs) in WS2 monolayers. These Vs can be either naturally formed during	(transition metals), WS2 monolayer with sulfur vacancies (Vs), H2S, S6, S8 (as common sulfur sources for	temperatur e, low concentrat ion of TM atoms, presence of sulfur vacancies	
anisotropy in two- dimensional materials: Transition-metal adatoms on defected tungsten	WS2	induced	template effect. The synthesis involves the creation of sulfur vacancies (Vs) in WS2 monolayers. These Vs can be either naturally formed during fabrication or	(transition metals), WS2 monolayer with sulfur vacancies (Vs), H2S, S6, S8 (as common sulfur sources for WS2	temperatur e, low concentrat ion of TM atoms, presence of sulfur vacancies	
anisotropy in two- dimensional materials: Transition-metal adatoms on defected tungsten	WS2	induced	template effect. The synthesis involves the creation of sulfur vacancies (Vs) in WS2 monolayers. These Vs can be either naturally formed during	(transition metals), WS2 monolayer with sulfur vacancies (Vs), H2S, S6, S8 (as common sulfur sources for	temperatur e, low concentrat ion of TM atoms, presence of sulfur vacancies	

processes.

The TM

atoms are

deposited

onto the Vs

sites, where

they are

strongly

anchored due

to high

binding

energies. The

deposition is

suggested to

be done at

low

temperature

and with a

low

concentration

of TM atoms

to prevent

clustering.

The surface

remains

reasonably

flat with TM

atoms slightly

sticking out

above the

sulfur plane

by a height of

0.15–0.40 Å.

A van der

Waals layer

such as

graphene or

hex-BN can

be added on

top to protect

the magnetic

units from

environmenta

1 interactions.

Protected giant magnetic	Os@D-	Defect-	Os atoms are	Os atoms,	Low	Not
anisotropy in two-	WS2	induced	deposited	WS2	temperatur	specified
dimensional materials:		synthesis	onto the	monolayer	e, low	1
Transition-metal adatoms		with Os	sulfur	with sulfur	concentrat	
on defected tungsten		atoms	vacancy (Vs)	vacancies	ion of Os	
disulfide monolayer			sites of D-	(Vs)	atoms,	
·		WS2. The Os	,	presence		
		atoms are		of sulfur		
			strongly		vacancies	
			anchored due		in WS2	
			to high			
			binding			
			energies. The			
			deposition is			
			done at low			
			temperature			
			and with a			
			low			
			concentration			
			of Os atoms			
			to prevent			
			clustering.			
			The Os atoms			
			slightly			
			protrude			
			above the			
			sulfur plane			
			by a height of			
			0.15–0.40 Å.			
			The resulting			
			structure has			
			a magnetic			
			anisotropy			
			energy			
			(MAE) of 45			
			meV, which			
			is sufficient to			
			overcome			
			thermal			
			fluctuations			
			for practical			
			applications.			
Protected giant magnetic	G/Os@D	Graphene-	A 5×5	Os atoms,	Fully	Not
anisotropy in two-	-WS2	adsorbed	graphene	WS2	relaxed	specified

dimensional materials:	Os@D-	supercell is	monolayer	atomic
Transition-metal adatoms	WS2	deposited on	with sulfur	structure
on defected tungsten	synthesis	a 4×4 Os@D-	vacancies	with van
disulfide monolayer	s y menesis	WS2	(Vs),	der Waals
disumae monorayer		supercell. The	graphene	correction
		atomic	graphene	term
		structure is		included
		fully relaxed		meraded
		with the		
		inclusion of		
		the van der		
		Waals		
		correction		
		term. The		
		graphene		
		layer aligns		
		its C–C		
		bridge site		
		with the Os		
		atom		
		underneath,		
		and the inter-		
		planar distance		
		between C		
		and S is about		
		3.3 Å. The Os		
		atoms are		
		pulled out by		
		0.11 Å by the		
		graphene		
		layer. The		
		resulting		
		structure has		
		a slightly		
		reduced MAE		
		of 38 meV		
		but still		
		remains		
		among the		
		largest .		
		reported.		

https://doi.org/10.1016/j.	T4,4,4-	First-	The synthesis	Carbon	Energy	Vienna ab
ssc.2019.02.001	graphyne	principles	method	atoms (sp	cutoff of	initio
		calculations	involves	and sp2	520 eV,	simulation
			designing a	hybridized).	energy	package
			new		precision	(VASP),
			structurally		of 10^-5	PHONOPY
			stable 2D		eV, 15 ×	code for
			carbon		15 × 1 Γ-	phonon
		network		centered	calculations	
			composed of		Monkhors	
			sp and sp2		t-Pack	
			hybridized		grid for	
			atoms using		Brillouin	
			first-		zone	
			principles		sampling,	
			calculations.		maximum	
			The		force on	
			calculations		each atom	
			are performed		less than	
			within the		$0.01~\mathrm{eV/Å}$	
			framework of		during	
			density		optimizati	
			functional		on,	
			theory (DFT)		vacuum	
			using the		space of at	
			Vienna ab		least 17 Å	
			initio		in the	
			simulation		perpendic	
			package		ular	
			(VASP). The		direction.	
			electron			
			exchange-			
			correlation			
			functional is			
			treated using			
			the			
			generalized			
			gradient			
			approximatio			
			n (GGA) with			
			the Perdew-			
			Burke-			
			Ernzerhof			
			(PBE)			

parameterizati

on. An energy

cutoff of 520

eV for the

plane wave

basis with an

energy

precision of

10^-5 eV is

used. The

first Brillouin

zone is

sampled with

a $15 \times 15 \times 1$

 Γ -centered

Monkhorst-

Pack grid.

During

geometry

optimization,

both atomic

positions and

lattice vectors

are fully

optimized

using the

conjugate

gradient

scheme until

the maximum

force on each

atom is less

than 0.01

eV/Å. A large

vacuum space

of at least 17

Å is applied

in the

perpendicular

direction of

the 2D layer

to avoid

image

interactions

	fugue the
	from the
	periodic
	boundary condition.
Evidence for Strain- single- mechanic	
Induced Local layer exfoliation	
Conductance graphene	manufactured specified), oxygen ,
Modulations in Single- on SiO2	via gold (for environme photolithog
Layer Graphene on SiO2	mechanical electrical nt at 400 raphic
	exfoliation. contacts) oC for 15 equipment,
	An optical minutes STM
	microscope (scanning
	was used to tunneling
	identify the microscope
	location of
	single-layer
	graphene, and
	photolithogra
	phic
	processes
	were
	employed to
	attach gold
	electrical
	contacts to
	the graphene.
	Prior to STM
	measurements
	, the sample
	was annealed
	in a high
	oxygen
	environment
	at
	temperatures
	of 400 oC for
	15 minutes to
	remove
	photoresist
	that remained
	from the
	photolithogra
	phy
	1 -

Dimensional Thermal-Hydraulic Analysis for a Packed Bed Regenerator Used in a Reheating Furnace	aluminu m oxide spheres (Al2O3)	Packed bed stuffing preparation	The packed bed is filled with aluminum oxide spheres (Al2O3) with a diameter of 13 mm. The flow length for a unit cell is 474 mm and the width is 10.2 mm. The physical properties of the packed stuffing, such as thermal conductivity and specific heat, are considered as functions of temperature and expressed as polynomials of temperature.	Aluminum oxide (Al2O3)	Operating temperatur e varies during furnace cycles; thermal conductivi ty and specific heat are temperatur e-dependent and modeled as polynomia ls.	Commercia l software (likely CFD- based) for simulation; no specific synthesis equipment is mentioned as the focus is on modeling and simulation.
	active MT liquid crystallin e phase	hierarchical assembly	Active MT liquid crystalline phase is synthesized by first polymerizing microtubules (MTs) with GMPCPP to a concentration of 6 mg/ml. The filaments are left at room	microtubule s (MTs), GMPCPP, biotin- labeled kinesin fragments (K401), tetrameric streptavidin, PEG (20kDa), phosphoeno l pyruvate (PEP),	MTs polymeriz ed at 6 mg/ml with GMPCPP; left at room temperatur e for 2 days to allow end- to-end annealing; ATP	convention al flow cell, fluorescenc e microscope , brightfield microscope

temperature concentrat pyruvate for 2 days to kinase/lactat ion allow end-tocontrolled dehydrogen end via annealing, ase regenerati ng system; resulting in an (PK/LDH), **PEG** average antilength of 1.5 bleaching induces μm. Biotinagents, 3 depletion labeled μm beads, interaction kinesin poly-Ls; samples fragments lysineobserved (401 amino poly(ethyle in a acids of the ne glycol) conventio N-terminal (PLL-PEG) nal flow motor domain block cell with of D. copolymers repulsive melanogaster polykinesin) are acrylamid purified from e-coated E. Coli. surfaces Motor clusters are assembled by mixing biotin-labeled K401 with tetrameric streptavidin at a molar ratio of 1.7:1. A nonadsorbing polymer, PEG (20kDa), is added to induce attractive interactions through the depletion mechanism, forming

extensile MT

bundles. The

system is

driven far

from

equilibrium

by adding an

ATP

regenerating

system

composed of

phosphoenol

pyruvate

(PEP) and

pyruvate

kinase/lactate

dehydrogenas

e (PK/LDH),

which

maintains

ATP

concentration

at a constant

level. The

active

mixtures also

include anti-

bleaching

agents. The

resulting

active MT

networks are

observed in a

conventional

flow cell with

surfaces

coated with a

repulsive

poly-

acrylamide

brush to

prevent

protein

adsorption.

The behavior

	of the active			
	samples is			
	monitored			
	using			
	fluorescence			
	microscopy			
	for MT			
	visualization			
	and			
	brightfield			
	microscopy			
	for tracking 3			
	μm beads			
	coated with			
	poly-L-			
	lysine-			
	poly(ethylene			
	glycol) (PLL-			
	PEG) block			
	copolymers to			
	suppress			
	sticking to			
	MT bundles.			
active emulsificati		BANs	aqueous	flat 2D oil-
active emaistread	1101110		aqaooas	1140 22 011
emulsion on	emulsion (e	extensile	nhase	water
emulsion on droplets	`	extensile AT	phase emulsified	water interface
emulsion on droplets	droplets are M	ЛΤ	emulsified	interface
	droplets are M created by bu	MT oundles),	emulsified in	interface setup,
	droplets are M created by bu dispersing Pl	MT oundles), PFPE-PEG-	emulsified in fluorinate	interface setup, emulsificati
	droplets are M created by bu dispersing Pl BANs in an Pl	MT oundles), PFPE-PEG- PFPE	emulsified in fluorinate d oil; MT	interface setup, emulsificati on system,
	droplets are More created by dispersing Pl BANs in an Pl aqueous su	MT oundles), PFPE-PEG- PFPE urfactant	emulsified in fluorinate d oil; MT bundles	interface setup, emulsificati on system, quasi-2D
	droplets are More created by dispersing Plans in an aqueous phase and (E	MT pundles), PFPE-PEG- PFPE urfactant E2K0660),	emulsified in fluorinate d oil; MT bundles adsorb	interface setup, emulsificati on system,
	droplets are created by but dispersing Pl BANs in an aqueous suphase and forming a flat 31	MT pundles), PFPE-PEG- PFPE urfactant E2K0660),	emulsified in fluorinate d oil; MT bundles adsorb onto	interface setup, emulsificati on system, quasi-2D
	droplets are More created by dispersing Plans in an aqueous phase and forming a flat 2D oil-water More dispersion of the created by the created by dispersion of the created by the create	MT pundles), PFPE-PEG- PFPE urfactant E2K0660), M HFE7500	emulsified in fluorinate d oil; MT bundles adsorb onto droplet	interface setup, emulsificati on system, quasi-2D
	droplets are created by but dispersing Pl BANs in an aqueous suphase and forming a flat 2D oil-water interface oil	MT pundles), PFPE-PEG- PFPE urfactant E2K0660), M HFE7500	emulsified in fluorinate d oil; MT bundles adsorb onto droplet surfaces;	interface setup, emulsificati on system, quasi-2D
	droplets are created by but dispersing Pl BANs in an aqueous phase and forming a flat 2D oil-water interface stabilized	MT pundles), PFPE-PEG- PFPE urfactant E2K0660), M HFE7500	emulsified in fluorinate d oil; MT bundles adsorb onto droplet surfaces; droplets	interface setup, emulsificati on system, quasi-2D
	droplets are created by bu dispersing Pl BANs in an aqueous su phase and forming a flat 2D oil-water interface stabilized with a	MT pundles), PFPE-PEG- PFPE urfactant E2K0660), M HFE7500	emulsified in fluorinate d oil; MT bundles adsorb onto droplet surfaces; droplets confined	interface setup, emulsificati on system, quasi-2D
	droplets are created by dispersing Pl BANs in an aqueous phase and forming a flat 2D oil-water interface stabilized with a surfactant.	MT pundles), PFPE-PEG- PFPE urfactant E2K0660), M HFE7500	emulsified in fluorinate d oil; MT bundles adsorb onto droplet surfaces; droplets confined to quasi-	interface setup, emulsificati on system, quasi-2D
	droplets are created by dispersing Pl BANs in an aqueous suphase and forming a flat 2D oil-water interface stabilized with a surfactant. The	MT pundles), PFPE-PEG- PFPE urfactant E2K0660), M HFE7500	emulsified in fluorinate d oil; MT bundles adsorb onto droplet surfaces; droplets confined to quasi- 2D	interface setup, emulsificati on system, quasi-2D
	droplets are created by dispersing Pl BANs in an aqueous phase and forming a flat 2D oil-water interface stabilized with a surfactant. The surfactant	MT pundles), PFPE-PEG- PFPE urfactant E2K0660), M HFE7500	emulsified in fluorinate d oil; MT bundles adsorb onto droplet surfaces; droplets confined to quasi- 2D chambers	interface setup, emulsificati on system, quasi-2D
	droplets are created by dispersing Pl BANs in an aqueous suphase and forming a flat 2D oil-water interface stabilized with a surfactant. The surfactant used is PFPE-	MT pundles), PFPE-PEG- PFPE urfactant E2K0660), M HFE7500	emulsified in fluorinate d oil; MT bundles adsorb onto droplet surfaces; droplets confined to quasi- 2D chambers or	interface setup, emulsificati on system, quasi-2D
	droplets are created by dispersing Pl BANs in an aqueous phase and forming a flat 2D oil-water interface stabilized with a surfactant. The surfactant used is PFPE-PEG-PFPE	MT pundles), PFPE-PEG- PFPE urfactant E2K0660), M HFE7500	emulsified in fluorinate d oil; MT bundles adsorb onto droplet surfaces; droplets confined to quasi- 2D chambers or spherical	interface setup, emulsificati on system, quasi-2D
	droplets are created by dispersing Pl BANs in an aqueous suphase and forming a flat 2D oil-water interface stabilized with a surfactant. The surfactant used is PFPE-PEG-PFPE (E2K0660) in	MT pundles), PFPE-PEG- PFPE urfactant E2K0660), M HFE7500	emulsified in fluorinate d oil; MT bundles adsorb onto droplet surfaces; droplets confined to quasi- 2D chambers or	interface setup, emulsificati on system, quasi-2D
	droplets are created by dispersing Pl BANs in an aqueous phase and forming a flat 2D oil-water interface stabilized with a surfactant. The surfactant used is PFPE-PEG-PFPE	MT pundles), PFPE-PEG- PFPE urfactant E2K0660), M HFE7500	emulsified in fluorinate d oil; MT bundles adsorb onto droplet surfaces; droplets confined to quasi- 2D chambers or spherical	interface setup, emulsificati on system, quasi-2D

			droplets are			
			encapsulated			
			in aqueous			
			phase			
			emulsified in			
			fluorinated			
			oil. When			
			confined to			
			quasi-2D			
			chambers or			
			spherical			
			surfaces, the			
			MT bundles			
			adsorb onto			
			the droplet			
			surfaces,			
			forming a			
			dense liquid			
			crystalline			
			monolayer.			
			The droplets			
			exhibit			
			autonomous			
			motility when			
			in frictional			
			contact with a			
			hard surface,			
			driven by			
			coherent			
			internal flows			
			generated by			
			the active MT			
			bundles.			
Facile assembly and	Fe2O3@	Preparation	The working	80 wt%	120 °C, 12	Scanning
electrochemical	GA	of	electrodes	Fe2O3, 10	h, vacuum	electron
properties of a-	composit	Fe2O3@G	were prepared	wt% super	oven	microscopy
Fe2O3@graphene	es	A	by mixing 80	P, 10 wt%		(SEM),
aerogel composites as		composites	wt% of active	PVDF,		Transmissi
electrode materials for		-	materials	NMP		on electron
lithium ion batteries			(Fe2O3), 10	solvent		microscopy
			wt% of super			(TEM), X-
			P as the			ray
			conductive			diffraction
			material, and			(XRD), N2
			,			, - /, - ·-

			10 wt% of			adsorption-
			polyvinyliden			desorption
			e fluoride			isotherms
			(PVDF) as			
			the binder in			
			N-			
			methylpyrroli			
			dinone			
			(NMP)			
			solvent to			
			form a slurry.			
			The slurry			
			was coated			
			onto a copper			
			foil and dried			
			at 120 °C for			
			12 h in a			
			vacuum oven.			
W2C/WS2 Alloy	W2C/WS	hydrotherm	The	W2C and	low	hydrotherm
Nanoflowers as Anode	2_4h	al method	W2C/WS2_4	WS2	temperatur	al reactor
Materials for Lithium-Ion			h alloy		e,	
Storage			nanoflowers		hydrother	
			(NFs) were		mal	
			successfully		conditions	
			fabricated via			
			a facile			
			hydrothermal			
			method at low			
			temperature.			
			The particle			
			size of the			
			NFs could be			
			controlled			
			between 200			
			nm and 1 μm.			
			The obtained			
			NFs exhibited			
			high purity			
			and well-			
			defined			
			hexagonal			
			structures of			
			W2C and			
			WS2. The			

,		control of reaction time			
		for the			
		preparation of			
		W2C/WS2			
		electrodes is			
		crucial to			
		optimize the			
		overall			
		electrochemic			
		al properties,			
		where the			
		W2C/WS2_4			
		h alloy is the			
		best			
		electrode.			
W2C/WS2 Alloy WS2 NF	synthesis of	The as-	WS2	0.1-3.0 V	not
Nanoflowers as Anode	WS2	prepared		voltage	specified
Materials for Lithium-Ion	nanoflower	WS2 NFs		range	
Storage	S	showed			
		lithiation at			
		0.5, 1.2, and			
		1.4 V,			
		attributing to			
		the reduction			
		of WS2 to			
		Li2S through			
		multiple			
		steps,			
		including the			
		formation of LixWS2 and			
		Lixw S2 and Li2S. The			
		WS2 NFs			
		were used as			
		anode			
		materials for			
		LIBs and			
		showed			
		charge and			
		discharge			
		capacities of			
		504.0 and			

			g-1,			
			respectively.			
Synthesis of PbCrO4	PbCrO4-	Hydrotherm	PbCrO4 was	K2Cr2O7 (5	150°C for	Teflon-
nanorods-Ti3C2Tx	MXene	al synthesis	prepared by	mmol),	20 h	lined
MXene composites: A	composit	of PbCrO4	hydrothermal	Pb(CH3CO	(hydrother	autoclave,
sensitive	e		method with	O)2 (5	mal),	centrifuge,
photoelectrochemical			slight	mmol),	60°C	vacuum
sensor for the detection			modification.	deionized	vacuum	dryer, tube
of cysteine in human			5 mmol	water (100	drying,	furnace
blood serum			K2Cr2O7	mL total),	300°C	
			was dissolved	methanol (1	annealing	
			in 50 mL	mL for	for 2 h	
			deionized	composite	(composit	
			water under	preparation)	e)	
			continuous			
			stirring to			
			form solution			
			A. 5 mmol			
			Pb(CH3COO)			
			2 was			
			dissolved in			
			50 mL			
			deionized			
			water under			
			continuous			
			stirring to			
			form solution			
			B. Solutions			
			A and B were			
			mixed at a 1:2			
			volume ratio			
			under			
			continuous			
			stirring. The			
			mixture was			
			transferred to			
			a Teflon-lined			
			80-mL			
			autoclave and			
			kept at 150°C			
			for 20 h. The			
			product was			
			centrifuged,			
			washed with			
			,, abited Witti			

			deionized			
			water, and			
			dried under			
			vacuum at			
			60°C			
			overnight.			
Synthesis of PbCrO4	PbCrO4-	Composite	100 mg of	PbCrO4	60°C	Ultrasonic
nanorods-Ti3C2Tx	MXene	preparation	PbCrO4, 1	(100 mg),	vacuum	bath,
MXene composites: A	composit	of PbCrO4-	mL of	MXene	drying,	centrifuge,
sensitive	e	MXene	monolayer	dispersion	300°C	vacuum
photoelectrochemical			MXene	(5 mg/mL, 1	annealing	dryer, tube
sensor for the detection			dispersion (5	mL),	for 2 h	furnace
of cysteine in human			mg/mL), and	methanol (1		
blood serum			1 mL	mL),		
			methanol	deionized		
			were	water (50		
			dispersed in	mL)		
			50 mL	•		
			deionized			
			water. The			
			mixture was			
			sonicated for			
			1.5 h,			
			centrifuged,			
			and washed			
			with water.			
			The			
			precipitate			
			was dried			
			overnight at			
			60°C under			
			vacuum. The			
			obtained			
			powder was			
			further			
			annealed in a			
			tube furnace			
			at 300°C for 2			
A ED CATEGORIA			h.	CAATTA		153.5
AFM/XPS Analysis of	C32H66	spin-	The C32H66	C32H66 at	Spin-	AFM
the Growth and	thin film	coating	thin films	concentratio	coating	(Atomic
Architecture of Oriented			were prepared	ns of 0.13%	process	Force
Molecular Monolayer by			by spin-	w/v and	with	Microscop
Spin Cast Process and Its			coating at	0.3% w/v	specific) for

Cross-Linking Induced			specific		concentrat	imaging
by Hyperthermal			concentration		ions of	and
Hydrogen			s (e.g., 0.13%		C32H66;	thickness
			w/v, 0.3%		cross-	estimation;
			w/v). The		linking	XPS (X-ray
			thickness of		was	Photoelectr
			the thin film		induced	on
			is controlled		by	Spectrosco
			by the		hyperther	py) for
			concentration		mal	surface
			and spin		hydrogen	chemical
			speed. The		bombardm	compositio
			films were		ent with	n and
			deposited on		fluence	thickness
			Si wafers and		higher	estimation;
			could be		than 5 ×	HHIC
			further treated		10^16/cm ²	(Hyperther
			with hexane		and	mal
			washing and		bombardm	Hydrogen
			hyperthermal		ent time	Ion
			hydrogen		up to 200	Bombardm
			bombardment		seconds.	ent)
			for cross-			equipment
			linking.			for cross-
			C			linking.
AFM/XPS Analysis of	С32Н66	Spin casting	C32H66 was	С32Н66,	Spin speed	Spin-
the Growth and	nanofilm		dissolved into	hexane	of 5000	coating
Architecture of Oriented			hexane under		rpm,	system
Molecular Monolayer by			magnetic		drying at	,
Spin Cast Process and Its			stirring, with		60°C for 4	
Cross-Linking Induced			its		h	
by Hyperthermal			concentration			
Hydrogen			varying from			
, 8			0.05% w/v to			
			0.5% w/v. A			
			50 μL			
			solution was			
			casted on a Si			
			wafer surface,			
			spun at 5000			
			rpm until it			
			-			
			transformed			
			transformed into a film,			

			C32H66			
			nanofilm was			
			obtained after			
			drying at			
			60°C for 4 h.			
AFM/XPS Analysis of	C32H66	Hypertherm	Cross-linking	Hydrogen	Kinetic	Home-
the Growth and	nanofilm	al	experiments	(H2)	energy of	made ECR-
Architecture of Oriented		hydrogen-	were		a few eV,	enhanced
Molecular Monolayer by		induced	conducted on		via	microwave
Spin Cast Process and Its		cross-	a home-made		electron	plasma
Cross-Linking Induced		linking	electron		cyclotron	reactor
by Hyperthermal		(HHIC)	cyclotron		resonance	
Hydrogen			resonance		(ECR)-	
			(ECR)-		enhanced	
			enhanced		microwav	
			microwave		e plasma	
			plasma		reactor	
			reactor, which			
			uses			
			extraction			
			ions to fill a			
			space fully			
			with H2 gas			
			to collide and			
			exchange its			
			kinetic energy			
			to hydrogen.			
			This process			
			may produce			
			H with some			
			certain kinetic			
			energy and/or			
			H2 having			
			more kinetic			
			energy. The			
			energetic			
			hydrogen			
			breaks C-H bonds and			
			then all C			
			radicals will			
			produce cross-linking.			

AFM/XPS Analysis of the Growth and Architecture of Oriented Molecular Monolayer by Spin Cast Process and Its Cross-Linking Induced by Hyperthermal Hydrogen	С32Н66	hypertherm al hydrogen bombardme nt	The synthesis method involves inducing cross-linking in C32H66 thin-film surfaces through hyperthermal hydrogen bombardment . This process is described in the context of both fully and partially cross-linked surfaces, indicating that the bombardment is used to manipulate the degree of cross-linking in the material.	Hydrogen (H2)	Hyperther mal energy conditions are applied to the thin film surface.	Atomic force microscopy (AFM) is used for imaging and analysis.
AFM/XPS Analysis of the Growth and Architecture of Oriented Molecular Monolayer by Spin Cast Process and Its Cross-Linking Induced by Hyperthermal Hydrogen	dotriacon tane	adsorption on SiO2 surface	Dotriacontane films are synthesized by adsorbing the alkane on a SiO2 surface. This is studied using high-resolution ellipsometry and synchrotron X-ray scattering techniques to	Dotriaconta ne (n- alkane)	Adsorption on a SiO2 surface under unspecified but controlled conditions.	Ellipsometr y, synchrotron X-ray scattering, and molecular dynamics simulations .

			understand the structure and growth mode of the film.			
AFM/XPS Analysis of the Growth and Architecture of Oriented Molecular Monolayer by Spin Cast Process and Its Cross-Linking Induced by Hyperthermal Hydrogen	dotriacon tane	vapor-phase growth	In-situ X-ray reflectivity is used to study the growth of alkane films from the vapor phase. This method allows for the investigation of molecular orientation and film structure during deposition.	Alkane molecules	Vapor- phase growth conditions	X-ray reflectivity equipment.
AFM/XPS Analysis of the Growth and Architecture of Oriented Molecular Monolayer by Spin Cast Process and Its Cross-Linking Induced by Hyperthermal Hydrogen	poly(tran s- isoprene)	hypertherm al proton cross- linking	A cross- linking route for poly(trans- isoprene) involves the use of hyperthermal protons, which induce molecular cross-linking through unusual collision kinematics. This method allows for the synthesis of tailor-made molecular films with controlled	Hypertherm al protons	Collision- induced cross- linking under low chemical- and energy- loads.	Atomic force microscopy (AFM) and other surface analysis techniques.

			chemical properties.			
AFM/XPS Analysis of the Growth and Architecture of Oriented Molecular Monolayer by Spin Cast Process and Its Cross-Linking Induced by Hyperthermal Hydrogen	dodecane thiol on Au(111)	hypertherm al proton bombardme nt	Hyperthermal proton bombardment is applied to study its effects on self-assembled monolayers of dodecanethiol on Au(111). This method is used to investigate changes in the monolayer structure and properties.	Dodecaneth iol, hypertherm al protons	Bombard ment under controlled hyperther mal proton conditions .	Atomic force microscopy (AFM) and surface science techniques.
AFM/XPS Analysis of the Growth and Architecture of Oriented Molecular Monolayer by Spin Cast Process and Its Cross-Linking Induced by Hyperthermal Hydrogen	alkane- metal- system (C32H66 /In)	STM investigations	Scanning tunneling microscopy (STM) is used to investigate the structure of the alkanemetal-system (C32H66/In). This method provides insights into the molecular arrangement and interactions at the interface.	C32H66, Indium (In)	Surface conditions suitable for STM imaging.	Scanning tunneling microscope (STM).
MXene-based promising nanomaterials for electrochemical energy storage	Ti3C2Tx	HF Etching	Ti3AlC2 MAX powder is added to hydrogen fluoride solution at	Ti3AlC2 MAX powder, hydrogen fluoride (HF)	Room temperatur e, pH ~6 after washing	Centrifuge, vacuum filtration

room

temperature.

The reaction

is exothermic,

requiring

gradual

addition of

MAX powder

to avoid

excessive

bubble

formation.

The etching

step produces

a 2D-

multilayered

structure. The

residue is

washed with

deionized

water to

remove AlF3

and

sedimentary

acids. After

centrifugation

and vacuum

filtration at

pH ~6, post-

processing

techniques

can customize

the final

product.

Surface

termination

with O, OH,

and F groups

occurs via

fluoride and

hydroxyl

ions.

MXene-based promising nanomaterials for electrochemical energy storage	Ti3C2Tx	Fluoride Salt Etching (LiF/HCl)	LiF and HCl are mixed, followed by gradual addition of Ti3AlC2 MAX powder. The etching is heated at 40°C for 45 hours. Byproducts (LiCl, AlF3) are removed by washing. Water addition, centrifugation, and decanting increase pH. The final clay-type paste is rolled into a flexible MXene film using a roller	LiF, HCl, Ti3AlC2 MAX powder	40°C, 45 hours	Roller mill
MXene-based promising nanomaterials for electrochemical energy storage	Ti3C2Tx	NH4HF2 Etching	using a roller mill. Ti3AlC2 MAX powder is treated with NH4HF2. The etching produces byproduct (NH4)3AlF6. Ammonium ions intercalate between Ti3C2Tx layers during the process.	NH4HF2, Ti3AlC2 MAX powder	Not explicitly stated	Not explicitly stated

			The final product forms thicker MXene films with larger inter-layer spaces due to intercalation.			
MXene-based promising nanomaterials for electrochemical energy storage	Ti3C2Tx	Alkali Treatment (NaOH)	Ti3AlC2 MAX powder is treated with strong alkaline compounds (NaOH). OH— ions oxidize Al into hydroxide, which dissolves in NaOH. Byproducts are removed via HF water solution and the Bayer process. High-temperature and high-alkali concentration conditions liquefy byproducts to facilitate Al layer	NaOH, Ti3AlC2 MAX powder	High temperatur e, high alkali concentrat ion	Not explicitly stated
MXene-based promising nanomaterials for electrochemical energy storage	Ti3C2Tx	NaOH etching	removal. Ti3C2Tx MXenes with 92 wt.% purity were fabricated by	27.5 M NaOH	270°C	Not specified

			treating Ti4AlN3 with 27.5 M NaOH at 270°C.			
MXene-based promising nanomaterials for electrochemical energy storage	Ti3C2Tx	Molten salt etching	Ti3C2Tx was synthesized by etching Ti3ZnC2 with ZnCl2 molten salt at 280°C (melting point) and 550°C. ZnCl2 ionizes into Zn ²⁺ and ZnCl4 ²⁻ , oxidizing Al to Al ³⁺ , forming AlCl3, and replacing Al with Zn.	ZnCl2	280°C (melting), 550°C (reaction), argon flow	Not specified
MXene-based promising nanomaterials for electrochemical energy storage	Ti3C2Tx	Electroche mical etching	Ti3C2Tx was produced via electrochemic al etching of Ti3AlC2 in a tetramethyla mmonium hydroxide (TMA-OH) and NH4Cl aqueous electrolyte. Cl ⁻ corroded Al, breaking Ti-Al bonds, and NH4OH further etched the material.	TMA-OH, NH4Cl	Aqueous electrolyte , anode setup	Electroche mical cell
MXene-based promising nanomaterials for	Ti3C2Tx	Bottom-up sputtering and etching	Ti3AlC2 thin films were deposited on	HF or NH4HF2	Not specified	Magnetron sputtering system

electrochemical energy			sapphire			
storage			substrates via			
			magnetron			
			sputtering,			
			followed by			
			etching with			
			HF or			
			NH4HF2 to			
			yield			
			Ti3C2Tx.			
MXene-based promising	Ti3ZnC2	Molten salt	Ti3ZnC2 was	ZnCl2	280°C	Not
nanomaterials for		etching	synthesized		(melting),	specified
electrochemical energy			by etching		550°C	
storage			with ZnCl2		(reaction),	
			molten salt at		argon flow	
			280°C and			
			550°C, where			
			Zn replaced			
			Al in the			
			MAX phase.			
MXene-based promising	Ti3C2Cl	Molten salt	Ti3C2Cl2	ZnCl2	280°C	Not
nanomaterials for	2	etching	was produced		(melting),	specified
electrochemical energy			by further		550°C	•
storage			etching		(reaction),	
_			Ti3ZnC2 with		argon flow	
			ZnCl2 molten			
			salt.			
MXene-based promising	Mo2CTx	Thermal	Mo2CTx was	HF	High	Thermal
nanomaterials for		deposition	synthesized		temperatur	deposition
electrochemical energy		and etching	by thermal		e, HF	system
storage			deposition of		etching	
			Mo2GaC on a			
			substrate,			
			followed by			
			HF etching to			
			remove Ga			
			layers.			
MXene-based promising	Mo2TiC	Bottom-up	Mo2TiC2Tx	Not	High	Thermal
nanomaterials for	2Tx	synthesis	was produced	specified	temperatur	deposition
electrochemical energy			via bottom-up		e	system
storage			methods			
			involving			
			thermal			
			deposition			

			and selective etching of MAX phases.			
10.1080/02786826.2014. 991438	graphene nanoflow ers (GNFs)	inductively annealing silicon- carbon (Si- C) nanoparticl es	Graphene nanoflowers (GNFs) were synthesized by inductively annealing silicon-carbon (Si-C) nanoparticles at 2600°C, as described in Miettinen et al. (2011, 2014). The powder was produced using industrially scalable processes.	silicon- carbon (Si- C) nanoparticle s	2600°C	inductively coupled annealing system
10.1080/02786826.2014. 991438	graphene nanoflow ers (GNFs)	ultrasonic spraying	Stable suspensions of GNFs were prepared in ethanol, DMF, and NMP. The suspensions were used to deposit micrometer- thick GNF films on glass substrates. The process involved an ultrasonic atomizer (Lechler, Type US 1)	ethanol, N,N- dimethylfor mamide (DMF), N- methyl-2- pyrrolidone (NMP)	150°C hot plate temperatur e, 9 L/min carrier gas flow rate, 10 cm spray distance, 200 mL/h suspensio n feeding rate, 7–14 min spraying time	ultrasonic atomizer (Lechler, Type US 1), syringe pump (Kd Scientific, KDS100), hot plate, plexiglass tube

			connected to			
			a syringe			
			pump (Kd			
			Scientific,			
			KDS100) and			
			operated at			
			100 kHz. A			
			carrier gas			
			flow rate of 9			
			L/min was			
			used to			
			transport the			
			droplets onto			
			the substrate.			
			The spray			
			distance was			
			10 cm, and			
			the			
			suspension			
			feeding rate			
			was 200			
			mL/h. The			
			hot plate			
			temperature			
			was set to			
			150°C (actual			
			measured			
			temperature			
			111°C). The			
			spraying time			
			varied			
			between 7			
			min and 14			
			min, with			
			some tests			
			using 30 s for			
			early			
			deposition			
			analysis.			
10.1080/02786826.2014.	multi-	inductively	Multi-layer	silicon-	2600°C	inductively
991438	layer	annealing	graphene	carbon (Si-		coupled
	graphene	silicon-	(MLG) flakes	C)		annealing
	(MLG)	carbon (Si-	were	nanoparticle		system
	flakes	C)	synthesized	S		-
			10			

_						
		nanoparticl	by			
		es	inductively			
			annealing			
			silicon-carbon			
			(Si-C)			
			nanoparticles			
			at 2600°C, as			
			described in			
			Miettinen et			
			al. (2011,			
			2014). The			
			powder was			
			produced			
			using			
			industrially			
			scalable			
			processes.			
10.1080/02786826.2014.	multi-	ultrasonic	Stable	ethanol,	150°C hot	ultrasonic
991438	layer	spraying	suspensions	N,N-	plate	atomizer
	graphene		of MLG	dimethylfor	temperatur	(Lechler,
	(MLG)		flakes were	mamide	e, 9 L/min	Type US
	flakes		prepared in	(DMF), N-	carrier gas	1), syringe
			ethanol,	methyl-2-	flow rate,	pump (Kd
			DMF, and	pyrrolidone	10 cm	Scientific,
			NMP. The	(NMP)	spray	KDS100),
			suspensions		distance,	hot plate,
			were used to		200 mL/h	plexiglass
			deposit		suspensio	tube
			micrometer-		n feeding	
			thick MLG		rate, 7–14	
			films on glass		min	
			substrates.		spraying	
			The process		time	
			involved an			
			ultrasonic			
			atomizer			
			(Lechler,			
			Type US 1)			
			connected to			
			a syringe			
			pump (Kd			
			Scientific,			
			KDS100) and			
			operated at			

			100 kHz. A			
			carrier gas			
			flow rate of 9			
			L/min was			
			used to			
			transport the			
			droplets onto			
			the substrate.			
			The spray			
			distance was			
			10 cm, and			
			the			
			suspension			
			feeding rate			
			was 200			
			mL/h. The			
			hot plate			
			temperature			
			was set to			
			150°C (actual			
			measured			
			temperature			
			111°C). The			
			spraying time			
			varied			
			between 7			
			min and 14			
			min, with			
			some tests			
			using 30 s for			
			early			
			deposition			
			analysis.			
10.1080/02786826.2014.	graphene	ultrasonic	GNF	0.05 wt%	Spraying	Ultrasonic
991438	nanoflow	spraying	suspensions	GNF	time of 7	sprayer
	ers		with a	suspension	min and	
	(GNFs)		concentration	in	14 min,	
			of 0.05 wt%	DMF/ethan	substrate	
			were	ol solvent	temperatur	
			ultrasonically	mixture	e of	
			sprayed onto		approxima	
			sprayed onto		"PPT GITTING	
			glass for 7		tely 111 C	

			films were		set to 150	
			prepared		C)	
			using a		<i>C)</i>	
			DMF/ethanol			
			solvent			
			mixture due			
			to its lower			
			boiling point			
			compared to			
			NMP. The			
			process			
			resulted in			
			percolated			
			films with			
			substrate			
			coverages of			
			approximatel			
			y 70% and			
			79% for 7-			
			min and 14-			
			min			
			depositions,			
			respectively.			
			The films			
			showed a			
			rough surface			
			due to the			
			inherently			
			irregular			
			shape of the			
			graphene			
			nanomaterials			
			nanomateriais			
10.1080/02786826.2014.	Multi-	ultrasonic	MLG	0.05 wt%,	Spraying	Ultrasonic
991438	Layer	spraying	suspensions	0.1 wt%,	time of 7	sprayer
,,,,,,,,,,,,,,,,,,,,,,,,,,,,,,,,,,,,,,,	Graphene	-178	with	and 0.2 wt%	min,	-FJ
	(MLG)		concentration	MLG	substrate	
	flakes		s of 0.05	suspension	temperatur	
			wt%, 0.1	in	e of	
			wt%, and 0.2	DMF/ethan	approxima	
			wt% were	ol solvent	tely 111 C	
			ultrasonically	mixture	(hot plate	
			sprayed for 7		set to 150	
			min onto		C)	
			IIIII OIIIO		<i>C)</i>	

			glass			
			substrates.			
			The films			
			were prepared			
			using a			
			DMF/ethanol			
			solvent			
			mixture. The			
			morphology			
			of MLG films			
			on glass was			
			investigated,			
			and the films			
			were found to			
			be composed			
			of compact			
			agglomerates			
			at higher			
			concentration			
			s. The process			
			resulted in a			
			substrate			
			coverage of			
			approximatel			
			y 79% for 0.2			
			wt% MLG			
			suspensions. The films			
			showed a			
			rough surface			
			due to the			
			irregular			
			shape of the			
			graphene			
			nanomaterials			
10 1000/0270/02/ 2014	C1	E14::	C1.	C1	C	E14
10.1080/02786826.2014.	Graphene	Electrospra	Graphene	Graphene	Spraying	Electrospra
991438	Nanoplat	y Danasitian	nanoplatelets	nanoplatelet	time of 14	y 1
	elets	Deposition	(GNF) are	s (GNF) in	minutes,	deposition
	(GNF)		deposited .	suspensions	0.05 wt%	equipment
			using		GNF	
			electrospray		suspensio	
			deposition.		ns	
			The process			
			52			

						-
			involves			
			suspensions			
			of GNF in			
			solvents and			
			is applied to			
			MA-glass			
			slides. The			
			spraying time			
			is critical,			
			with nearly			
			100%			
			substrate			
			coverage			
			achieved at			
			14 minutes of			
			spraying			
			using 0.05			
			wt% GNF			
			suspensions. The method			
			inherently involves			
			rotation of			
			individual			
			graphene			
			layers with			
			respect to			
			each other, as			
			revealed by			
			Raman			
			spectra.			
10.1080/02786826.2014.	Few-	Synthesis in	Few-layer	Graphene	Ethanol-	Chemical
991438	Layer	Ethanol-	graphene	precursors	soluble	synthesis
	Graphene	Soluble	nanosheets	for	conditions	and
	Nanoshe	Dispersions	are	exfoliation		dispersion
	ets		synthesized			equipment
			using a			
			chemical			
			route that			
			allows them			
			to be ethanol-			
			soluble. This			
			method is			
			used to			
			F2			

			produce			
			flexible and			
			transparent			
			conducting			
			composite			
			films. The			
			process			
			involves			
			chemical			
			exfoliation			
			and			
			dispersion			
			techniques to			
			achieve the			
			desired			
			solubility and			
			film			
			properties.			
10.1080/02786826.2014.	N-Doped	Chemical	N-doped	Graphene	Condition	Chemical
991438	Graphene	Doping and	graphene	precursors	s for	synthesis
	Nanoplat	Exfoliation	nanoplatelets	and	exfoliation	and
	elets		are	nitrogen-	and	exfoliation
			synthesized	doping	nitrogen	equipment
			through a	agents	doping	1 1
			chemical	8	1 8	
			doping			
			process			
			involving			
			nitrogen			
			incorporation.			
			The method is			
			The method is used to create			
			The method is used to create superior			
			The method is used to create superior metal-free			
			The method is used to create superior metal-free counter			
			The method is used to create superior metal-free counter electrodes for			
			The method is used to create superior metal-free counter electrodes for organic dye-			
			The method is used to create superior metal-free counter electrodes for organic dyesensitized			
			The method is used to create superior metal-free counter electrodes for organic dyesensitized solar cells.			
			The method is used to create superior metal-free counter electrodes for organic dyesensitized solar cells. The process			
			The method is used to create superior metal-free counter electrodes for organic dyesensitized solar cells. The process includes			
			The method is used to create superior metal-free counter electrodes for organic dyesensitized solar cells. The process includes exfoliation			
			The method is used to create superior metal-free counter electrodes for organic dyesensitized solar cells. The process includes			

			achieve the desired electronic properties.			
10.1080/02786826.2014.	Reduced Graphene Oxide Sheets	Covalent Assembly	Reduced graphene oxide sheets are synthesized via covalent assembly on a silicon substrate. This method involves chemical functionalizat ion and assembly to produce the graphene sheets. The process is used to study tribology on silicon substrates.	Graphene oxide and functionaliz ing agents	Chemical conditions for covalent assembly	Chemical synthesis and coating equipment
10.1080/02786826.2014. 991438	Silicon– Carbon Nanocera mics	Atmospheri c Pressure Chemical Vapour Synthesis	Silicon— carbon nanoceramics are synthesized using atmospheric pressure chemical vapour synthesis from hexamethyldi silane in a high- temperature aerosol	Hexamethyl	High- temperatur e aerosol reactor, atmospher ic pressure	High- temperature aerosol reactor

			reactor. The method involves the decompositio n of hexamethyldi silane at high temperatures to form the nanoceramics .			
10.1080/02786826.2014. 991438	Graphene Oxide Films	Electrospra y Deposition and Post- Annealing	Graphene oxide films are synthesized using electrospray deposition followed by post- annealing. The electrospray process deposits the graphene oxide, and the post- annealing step enhances crystallinity and reduces defects. The sensitivity of the micro- Raman spectrum to the crystallite size of the films is studied.	Graphene oxide	Electrospr ay deposition parameter s and post- annealing conditions	Electrospra y deposition system and annealing furnace
10.1080/02786826.2014. 991438	Graphene -Based	Electrodyna mically	Graphene- based thin films are	Graphene nanosheets	Electrody namic	Electrospra y

	Thin	Sprayed	synthesized		spraying	deposition
	Films	Deposition	using		conditions	system
		1	electrodynami			J
			cally sprayed			
			deposition.			
			This method			
			is used for			
			device			
			applications			
			and involves			
			the controlled			
			deposition of			
			graphene			
			nanosheets to			
			form thin			
			films with			
			specific			
			properties.			
10.1080/02786826.2014.	Nickel	Spray	Nickel oxide-	Nickel	Spray	Spray
991438	Oxide-	Pyrolysis	gadolinia	oxide and	pyrolysis	pyrolysis
	Gadolini		doped ceria	gadolinia	conditions	system
	a Doped		composite	doped ceria	involving	
	Ceria		thin films are	precursors	the	
	Composit		synthesized		Leidenfros	
	e Thin		using spray		t effect	
	Films		pyrolysis. The			
			method			
			involves the			
			Leidenfrost			
			effect during			
			the deposition			
			process,			
			which affects the film			
			formation and			
			properties.			
			The process is			
			used to create			
			composite			
			thin films			
			with specific			
			functionalities			
			•			

10.1080/02786826.2014.	Zirconia	Electrostati	Zirconia	Zirconia	Electrostat	Electrostati
991438	Coatings	c Spray	coatings are	precursors	ic spray	c spray
		Deposition	synthesized		deposition	deposition
		(ESD)	using		parameter	system
			electrostatic		S	
			spray			
			deposition			
			(ESD). The			
			method			
			involves the			
			application of			
			an electric			
			field to			
			deposit			
			zirconia			
			particles onto			
			a substrate.			
			The initial			
			stages of			
			coating			
			formation are			
			studied to			
			understand			
			the process			
			parameters			
			and their			
			effects on the			
			final film			
			properties.			
10.1080/02786826.2014.	Graphene	Chemical	Graphene	Graphene	Chemical	Chemical
991438	Nanoshe	Route	nanosheets	precursors	exfoliation	synthesis
	ets		are	and	and	and
			synthesized	chemical	functionali	exfoliation
			via a	exfoliation	zation	equipment
			chemical	agents	conditions	1 1
			route suitable	8		
			for device			
			applications.			
			The method			
			involves			
			chemical			
			exfoliation			
			and			
			functionalizat			
			runchonanzat			

10.1080/02786826.2014. 991438	Graphene Oxide Films	Low Temperatur e Reduction with Vanadium(I II)	ion to produce nanosheets with specific properties for integration into devices. Graphene oxide films are synthesized and then reduced at low temperatures using vanadium(III) . The reduction process is	Graphene oxide, vanadium(II I)	Low- temperatur e reduction conditions	Reduction furnace or low- temperature reactor
0.1038/s41598-020-	WS2	CVD	vanadium(III) . The reduction	Not	Not	Not
68321-7		synthesis	synthesis method is used to produce WS2 films, which favor small grains (~10 nm²), but larger grains up to approximatel	specified in the text	specified in the text	specified in the text

			y 100 nm² are also present.			
10.1038/s41598-020- 68321-7	WS2	ALD and gas conversion	2 nm of WO3 is deposited using ALD onto 30 nm thick electron transparent Si3N4 TEM windows. The WO3 is then converted to WS2 by flowing H2S gas over the films at elevated temperature.	WO3, H2S gas	Elevated temperatur e	ALD system, electron transparent Si3N4 TEM windows
10.3390/biomedicine901 0080	DOX/Pd @ZIF- 8@PDA	self- assembled one-pot method	DOX, Pd, and ZIF-8 were conjugated in a self-assembled one-pot method, and then coated with PDA to improve biocompatibil ity.	DOX, Pd, ZIF-8, PDA	Not specified in the provided text	Not specified in the provided text
10.3390/biomedicine901 0080	MoS2- PEG nanoshee t	Preparation of MoS2- PEG nanosheet	The nanosheets were prepared by loading doxorubicin (DOX) onto MoS2-PEG. The nanosheets were analyzed for drug delivery and photothermal	Doxorubici n (DOX), MoS2, PEG	NIR irradiation	Not specified

			effects by NIR irradiation.			
10.3390/biomedicine901 0080	MnO2- PEG- cRGD/C e6	Preparation of MnO2- PEG- cRGD/Ce6	Ultrathin MnO2 nanosheets were prepared with polyethylene glycol-cyclic arginine- glycine- aspartic acid tripeptide (PEG-cRGD) and encapsulated chlorin e6 (Ce6). The nanosheets showed photothermal efficiency of 39% and pH- controlled Ce6 release under a 660 nm NIR laser.	MnO2, PEG-cRGD, chlorin e6 (Ce6)	pH-controlled release, 660 nm NIR laser	Not specified
10.3390/biomedicine901 0080	TiL4@B PQDs	Fabrication of TiL4@BPQ Ds	TiL4 was coordinated with black phosphorus quantum dots (BPQDs) to enhance their stability in aqueous dispersions. The TiL4@BPQD s were used for PA imaging of cancer cells	TiL4, black phosphorus quantum dots (BPQDs)	Aqueous dispersion	Not specified

			and xenografted tumors in mice.			
10.3390/biomedicine901 0080	ICG-rGO nanocom posite	Fabrication of ICG-rGO nanocompo site	Indocyanine green (ICG) was conjugated to reduced graphene oxide (rGO) to create a nanocomposit e for dual use in PA imaging and fluorescence imaging. The nanocomposit e showed high PA/fluorescen ce signals and strong tumor accumulation.	Indocyanine green (ICG), reduced graphene oxide (rGO)	NIR regime	Not specified
10.3390/biomedicine901 0080	AMNFs (Antimon y nanoflak es)	Liquid phase exfoliation of AMNFs	AMNFs were fabricated via liquid phase exfoliation of bulk antimony (Sb). The nanoflakes exhibited unique PA properties and high PT conversion efficiency (42.36%).	Bulk antimony (Sb)	Liquid phase exfoliation	Not specified
10.3390/biomedicine901 0080	Sb2Se3 nanoshee ts	Fabrication of Sb2Se3 nanosheets	Sb2Se3 nanosheets were fabricated	Antimony (Sb), Selenium (Se)	Liquid nitrogen pretreatme nt, freeze-	Not specified

			using liquid		thawing	
			nitrogen		approach	
			pretreatment			
			and a freeze-			
			thawing			
			approach. The			
			nanosheets			
			had an			
			extinction			
			coefficient of			
			33.2 L/g⋅cm			
			and a			
			photothermal			
			conversion			
			efficiency of			
			30.78%.			
10.3390/biomedicine901	Ti3C2	Exfoliation	Ti3C2	MAX-phase	Exfoliatio	Not
0080	MXene	of Ti3C2	MXene was	ceramics	n from	specified
		MXene	exfoliated		MAX-	
			from layer-		phase	
			structured		ceramics	
			MAX-phase			
			ceramics. The			
			nanosheets			
			exhibited a			
			PA signal at			
			an excitation			
			wavelength of			
			808 nm in			
			vitro and a			
			significant			
			increase in			
			PA signal at a			
			concentration			
			of 15 mg/kg			
			in tumor-			
			bearing mice.			
10.3390/biomedicine901	SP-	Fabrication	SP-modified	MnOx,	Subcutane	Not
0080	MnOx/T	of SP-	MnOx/Ta4C3	Ta4C3, SP	ous	specified
	a4C3	MnOx/Ta4	-based	(stabilizing	administra	
	composit	C3	nanosheets	agent)	tion	
	e	composite	were			
	nanoshee	nanosheets	fabricated.			
	ts		The			

			nanosheets			
			showed fast			
			enhanced PA			
			signals after			
			subcutaneous			
			administratio			
			n in 4T1			
			tumor-bearing			
			mice and			
			exhibited			
			contrast-			
			enhanced			
			properties in			
			CT and MR.			
10.3390/biomedicine901	PVP-	Fabrication	PVP-	Bi2Se3,	808 nm	Not
0080	Bi2Se3	of PVP-	encapsulated	PVP	excitation	specified
0000	nanoshee	Bi2Se3	Bi2Se3	(polyvinyl	wavelengt	specificu
	ts	nanosheets	nanosheets	pyrrolidone)	h, 5 h	
	ts	nanosneets	were	pyrrondone)	post-	
			fabricated.		-	
			The		injection	
			nanosheets			
			had an			
			extinction			
			coefficient of			
			11.5 L/g·cm			
			at 808 nm, a			
			PT			
			conversion			
			efficiency of			
			34.6%, and			
			excellent			
			photoacoustic			
			performance			
			with a			
			twofold			
			increase after			
			5 h of			
			injection.			
10.3390/biomedicine901	HA-	Fabrication	НА	MoS2, HA	pH and	Not
0080	MoS2	of HA-	(hyaluronic	(hyaluronic	GSH-	specified
	nanoshee	MoS2	acid) was	acid)	induced	
	ts	nanosheets	conjugated to		intracellul	
			MoS2		ar	

			nanosheets to		disulfide	
			induce HA		cleavage	
			receptor-			
			mediated			
			endocytosis.			
			The			
			nanosheets			
			were			
			internalized			
			via CD44,			
			HARE, and			
			LYVE-1			
			receptors, and			
			showed a			
			1860-fold			
			increase in			
			PA signal in			
			tumor-bearing			
			mice.			
10.3390/biomedicine901	Pd	Fabrication	Pd nanosheets	Palladium	NIR	Not
0080	nanoshee	of Pd	were	(Pd)	absorption	specified
	ts	nanosheets	fabricated as	(- 1)	r	-F
	.	114110011001	typical 2D			
			nanomaterials			
			with well-			
			defined and			
			controllable			
			sizes. The			
			nanosheets			
			were used for			
			PA-guided			
			PTT due to			
			their strong			
			NIR			
			absorption and excellent			
			biocompatibil			
Multilayorad ayanasant	MoS2	Coating	ity.	MoS2	Near-	Fibor ontic
Multilayered evanescent		Coating	A 5-layer		near- infrared	Fiber optic
wave absorption based	monolay		sensor design	monolayer,		sensor
fluoride fiber sensor with	er		is simulated	α-Si layer	(NIR)	system with
2D material and			with a MoS2	(10 nm	spectral	5-layer
amorphous silicon layers			monolayer	thick),	region, $\lambda =$	configurati
for enhanced sensitivity			coated over a	ZBLA core,	0.954 μm,	on (ZBLA

and resolution in near	10 nm thick	19.3%	$\lambda = 1.236$	core –
infrared	α-Si layer.	GeO2	μ m, λ =	19.3%
	The sensor is	doped silica	1.55 μm	GeO2
	analyzed for	clad, H2O	·	doped silica
	its	as reference		clad –
	performance	analyte,		MoS2
	in the near-	HCC tissue		monolayer
	infrared	as analyte		– α-Si layer
	(NIR)	·		– analyte)
	spectral			
	region for			
	detecting			
	malignancy in			
	liver tissues			
	through			
	variations in			
	their			
	refractive			
	index (RI)			
	values. The			
	sensitivity			
	and resolution			
	are evaluated			
	for different			
	configuration			
	s, including			
	varying the			
	thickness of			
	the α -Si layer			
	and the			
	cladding			
	material. The			
	dispersion			
	relation of			
	H2O is			
	considered as			
	a reference			
	analyte,			
	which leads			
	to improved			
	sensitivity			
	and resolution			
	compared to			
	using N tissue			

			as a			
			reference.			
			The			
			maximum			
			sensitivity			
			values (Sr, Si)			
			for H2O-			
			HCC			
			detection are			
			reported as			
			(225.5			
			mW/RIU,			
			1182.9			
			mW/RIU) at			
			$\lambda = 0.954 \mu\text{m}.$			
Multilayered evanescent	4-layer	Simulation	A 4-layer	ZBLA core,	Near-	Fiber optic
wave absorption based	sensor		sensor design	19.3%	infrared	sensor
fluoride fiber sensor with	design		is simulated	GeO2	(NIR)	system with
2D material and	with 10		without a 2D	doped silica	spectral	4-layer
amorphous silicon layers	nm thick		material,	clad (10 nm	region, λ =	configurati
for enhanced sensitivity	α-Si		consisting of	thick),	1.236 μm	on (ZBLA
and resolution in near	layer		a ZBLA core,	analyte	11 2 00 pini	core –
infrared	iayei		19.3% GeO2	unary to		19.3%
mmurod			doped silica			GeO2
			clad (10 nm			doped silica
			thick), and			clad –
			analyte. The			analyte)
			sensitivity			anaryte)
			and resolution			
			are compared			
			with the 5-			
			layer sensor			
			design with			
			MoS2 and α-			
			Si layers. At λ			
			= $1.236 \mu \text{m}$,			
			•			
			the sensitivity			
			values (Sr, Si)			
			are reported			
			as (110.3			
			mw/RIU,			
			647.8			
			mw/RIU).			

Multilayered evanescent wave absorption based fluoride fiber sensor with 2D material and amorphous silicon layers for enhanced sensitivity and resolution in near infrared	5-layer sensor design with 10 nm thick α-Si layer	Simulation with MoS2 and α-Si layers	A 5-layer sensor design is simulated with a ZBLA core, 19.3% GeO2 doped silica clad, a MoS2 monolayer, a 10 nm thick α -Si layer, and analyte. The sensor is analyzed for sensitivity and resolution in the NIR region. The sensitivity values (Sr, Si) at $\lambda = 1.236$ μ m are (123.0 mw/RIU), and the resolution values (Rr, Ri) are (8.13 \times 10–10 RIU, 1.53 \times 10–10 RIU). The sensor design with 10 nm α -Si layer shows a 11.5% enhancement in Sr compared to the 4-layer	ZBLA core, 19.3% GeO2 doped silica clad, MoS2 monolayer, α-Si layer (10 nm thick), analyte	Near-infrared (NIR) spectral region, λ = 1.236 μm	Fiber optic sensor system with 5-layer configurati on (ZBLA core – 19.3% GeO2 doped silica clad – MoS2 monolayer – α-Si layer – analyte)
			compared to the 4-layer			
			sensor without α -Si.			

for enhanced sensitivity and resolution in near infrared	α-Si layer and H2O as reference analyte	GeO2 doped silica clad, a MoS2 monolayer, a 10 nm thick α -Si layer, and H2O as the reference analyte. The sensitivity and resolution are evaluated for both real and imaginary parts of HCC tissue RI. At $\lambda = 0.954 \mu m$, the sensitivity values (Sr, Si) are (225.5 mW/RIU, 1182.9 mW/RIU), and the resolution values (Rr, Ri) are (4.43 \times 10–10 RIU, 8.85 \times 10–11 RIU). This design is found to provide 1.8 times better	monolayer, α-Si layer (10 nm thick), H2O as reference analyte, HCC tissue as analyte	0.954 μm	configurati on (ZBLA core – 19.3% GeO2 doped silica clad – MoS2 monolayer – α-Si layer – analyte)
		provide 1.8			

design. 10.1021/acsnano.2c0106 MoS2 High- pressure MoS2 Raman and samples w photolumin prepared v escence chemical (PL) vapor experiments deposition (CVD) on SiO2/Si substrates loaded into diamond anvil cell (DAC) usi the horses method. A 2.33 eV	r Methanol, Temperatu Diamond
excitation laser was used at 10 to collect Raman an PL spectra 4:1 methanol/ nol mixtur was used a the pressur transmittir medium (PTM). Pressure w determined situ using low- temperatur ruby fluorescen calibration	ethanol, re: 10 K, anvil cell vere 2.33 eV Pressure: (DAC), via excitation 0-4.5 Raman laser GPa, spectromete Atmosphe r, re: photolumin to Hydrostati escence c pressure setup, 2.33 and using eV laser DAC K d a. A etha re as re ng vas d in a re
10.1021/acsnano.2c0106 WSe2 High- Monolaye 5 pressure WSe2 Raman and samples w	ethanol, re: 10 K, anvil cell

		photolumin escence (PL) experiments	prepared via chemical vapor deposition (CVD) onto SiO2/Si substrates and loaded into a diamond anvil cell (DAC) using the horseshoe method. A 2.33 eV excitation laser was used at 10 K to collect Raman and PL spectra. A 4:1 methanol/etha nol mixture was used as the pressure transmitting medium (PTM). Pressure was determined in	excitation	0-4.5 GPa, Atmosphe re: Hydrostati c pressure using DAC	Raman spectromete r, photolumin escence setup, 2.33 eV laser
10.1021/acsnano.2c0106	MoS2	metal-orga	Pressure was determined in situ using a low-temperature ruby fluorescence calibration. Monolayer	molybdenu	low	one-inch
5		nic chemical vapor deposition (MOCVD)	MoS2 flakes were synthesized on a 300 nm- thick SiO/Si wafer using a one-inch	m hexacarbon yl (Mo(CO)6), diethyl sulfide ((C2H5)2S),	pressure, growth temperatur e below 350 °C, growth time of 6 h	quartz tube furnace, bubbler system

		quantz tulea	Ar carrier		
		quartz tube furnace under			
			gas		
		low pressure. The			
		precursors			
		used were			
		molybdenum			
		hexacarbonyl			
		(Mo(CO)6)			
		and diethyl			
		sulfide			
		((C2H5)2S).			
		The synthesis			
		was carried			
		out with an			
		Ar carrier gas			
		flow rate of			
		100 sccm, 0.1			
		scem for			
		Mo(CO)6,			
		and 1.0 sccm			
		for			
		(C2H5)2S.			
		The growth			
		temperature			
		was below			
		350 °C, and			
		the growth			
		time was 6			
		hours.			
10.1021/acsnano.2c0106 WSe2	metal-orga	Monolayer	tungsten	low	one-inch
5	nic	WSe2 flakes	hexacarbon	pressure,	quartz tube
	chemical	were	yl	growth	furnace,
	vapor	synthesized	(W(CO)6),	temperatur	bubbler
	deposition	using a one-	dimethyl	e of	system
	(MOCVD)	inch quartz	selenide	420 °C,	
		tube furnace	((CH3)2Se),	growth	
		under low	Ar carrier	time of 5 h	
		pressure. The	gas, H2		
		precursors			
		used were			
		tungsten			
		hexacarbonyl			

			dimethyl			
			selenide			
			((CH3)2Se),			
			and hydrogen			
			(H2). The			
			synthesis was			
			carried out			
			with an Ar			
			carrier gas			
			flow rate of			
			100 sccm, 1			
			sccm for H2,			
			0.3 sccm for			
			W(CO)6, and			
			0.05 sccm for			
			(CH3)2Se.			
			The growth			
			temperature			
			was 420 °C,			
			and the			
			growth time			
			was 5 hours.			
10.1021/acsnano.2c0106	monolay	chemical	The synthesis	molybdenu	low	chemical
5	er MoS2	vapor	of high-	m and	temperatur	vapor
		deposition	performance	sulfur	e	deposition
			monolayer	precursors		system
			molybdenum			
			disulfide is			
			achieved at			
			low			
			temperature			
			using			
			chemical			
			vapor			
			deposition			
			(CVD).			
10.1021/acsnano.2c0106	monolay	chemical	Monolayer	molybdenu	not	chemical
5	er MoSe2	vapor	MoSe2	m and	explicitly	vapor
		deposition	devices are	selenium	mentioned	deposition
		•	fabricated by	precursors		system,
			the pick-up of	-		hBN
			pre-patterned			(hexagonal
			hBN,			boron
			enabling			nitride) for
			0			,

			encapsulation and precise electronic transport studies.			encapsulati on
10.1021/acsnano.2c0106 5	monolay er WSe2	chemical vapor deposition	Monolayer WSe2 is studied in the context of interlayer excitons and their control through low- temperature photocurrent spectroscopy.	tungsten and selenium precursors	low temperatur e	chemical vapor deposition system
10.1021/acsnano.2c0106 5	few-layer graphene	compressio n	A hard, transparent, sp3- containing 2D phase is formed from few-layer graphene under compression.	few-layer graphene	high pressure	compressio n apparatus
	monolay er MoS2	chemical vapor deposition (CVD)	A monolayer MoS2 sample was grown using chemical vapor deposition (CVD). The lattice coefficient of MoS2 is 0.27 nm. This method can be adapted to use other monolayer two- dimensional	Not specified in the text.	Not specified in the text.	STEM probe, camera length of 20 cm, 80 kV accelerating voltage.

monolay	Aberration	materials by changing the two-dimensional lattice parameter used for the analysis.	monolayer	acceleratin	JEM-
er graphene	measureme nt using Ronchigra m	Ronchigram was recorded at an accelerating voltage of 80 kV from a monolayer graphene sample on a Gatan Oneview camera with 4096 x 4096 pixels using a focused STEM probe. The Ronchigram was divided into local angular areas, and the lateral magnification change in two directions for each segment was measured using an auto- correlation function. The positions of the maxima of three peaks in the auto- correlation	graphene	g voltage of 80 kV, camera length of 40 cm, focused STEM probe	ARM300F electron microscope, Gatan Oneview camera, aberration correctors

		function were			
		located to			
		sub-pixel			
		accuracy with			
		parabolic fits			
		and fitted to			
		an oval			
		function.			
		From these			
		fitted			
		parameters,			
		the aberration			
		coefficients			
		for the probe-			
		forming lens			
		were			
		calculated			
		using the			
		known lattice			
		parameter of			
		graphene and			
		the camera			
		length.			
Tin Compensation for the SnS file	m MBE	The SnS film	Hydrochlori	Diluted	MBE
SnS Based	technique	was deposited	c acid	HC1	chamber,
Optoelectronic Devices	•	onto a silicon-	(HCl),	solution	E-beam
•		doped	deionized	(HCl:H2O	evaporation
		gallium	water	= 1:1), 1	technique
		nitride		minute	for Ni
		(GaN:Si)		dipping	electrode
		layer. The		time	deposition,
		GaN:Si layer			shadow
		was grown on			mask with
		a sapphire			square
		substrate and			openings
		pre-treated by			$(2 \times 2 \text{ mm}2)$
		dipping into)
		diluted			,
		hydrochloric			
		acid			
		(HCl:H2O =			
		1:1) for 1			
		minute to			

			native oxide			
			layer,			
			followed by			
			rinsing with			
			deionized			
			water before			
			being			
			transferred			
			into the MBE			
			chamber.			
Tin Compensation for the	GaN:Si	MBE	A 2 μm thick	Silicon-	Thickness	MBE
SnS Based	layer	growth	GaN:Si	doped	of 2 μm	technique
Optoelectronic Devices	•		window layer	gallium	•	•
•			was grown on	nitride		
			a sapphire	(GaN:Si)		
			substrate. The			
			GaN:Si layer			
			was used as			
			an n-type			
			window			
			electrode in			
			the			
			SnS/GaN:Si			
			heterojunctio			
			n device.			
Tin Compensation for the	Ni	E-beam	A shadow	Nickel (Ni)	Thickness	E-beam
SnS Based	electrode	evaporation	mask with		of 120 nm	evaporation
Optoelectronic Devices	S		square			technique,
			openings			shadow
			$(2 \times 2 \text{ mm2})$			mask with
			was used to			square
			deposit			openings
			120 nm thick			$(2 \times 2 \text{ mm}2)$
			Ni electrodes)
			by E-beam			
			evaporation			
			technique.			
Tin Compensation for the	SnS	van der	Highly	Sn and S	Not	MBE
SnS Based		Waals	textured SnS	(not	explicitly	system
Optoelectronic Devices		epitaxy	was grown on	specified in	mentioned	
			mica	detail in the	in the	
			substrate	main text,	main text.	
			using a MBE	but implied		
			system.	by the		

Tin Compensation for the SnS Based Optoelectronic Devices	SnS	chemical vapor deposition	SnS nanowires were synthesized via chemical vapor deposition.	context of MBE system usage). Not explicitly mentioned in the main text.	Not explicitly mentioned in the main text.	Chemical vapor deposition system
Tin Compensation for the SnS Based Optoelectronic Devices	SnS	congruent thermal evaporation	3.88% Efficient Tin Sulfide Solar Cells were fabricated using congruent thermal evaporation.	Sn and S (implied by the context of SnS solar cells).	Not explicitly mentioned in the main text.	Thermal evaporation system
Tin Compensation for the SnS Based Optoelectronic Devices	SnS	co- evaporation	Tin sulphide thin films were synthesized by co- evaporation.	Sn and S (implied by the context of tin sulphide thin films).	Not explicitly mentioned in the main text.	Co- evaporation system
Tin Compensation for the SnS Based Optoelectronic Devices	SnS	heating Se- Sn layers	Semiconducti ng tin selenide thin films were prepared by heating Se-Sn layers.	Se and Sn	Heating process	Heating apparatus
	FeSe monolay er films	Thin film growth on SrTiO3 substrates	Monolayer films of FeSe were grown on 0.05 wt% Nb-doped SrTiO3 substrates. The substrates were degassed for	Fe (99.98%), Se (99.999%)	Degassing at 600 °C for 2 h, annealing at 925 °C for 12 min, growth at 300 °C, postgrowth	Knudsen cells, quartz crystal balance, reflection high-energy electron diffraction, ARPES chamber

			2 h at 600 °C		annealing	
			and then		at 350 °C	
			annealed for		for 20 h	
			12 min at			
			925 °C. Fe			
			(99.98%) and			
			Se (99.999%)			
			were co-			
			evaporated			
			from			
			Knudsen cells			
			with a flux			
			ratio of 1:10,			
			measured by			
			a quartz			
			crystal			
			balance, and a			
			growth rate of			
			0.31 unit cell			
			per minute.			
			The growth			
			process was			
			monitored			
			using			
			reflection			
			high-energy			
			electron			
			diffraction.			
			After growth,			
			the FeSe			
			monolayer			
			films were			
			annealed at			
			350 °C for 20			
			h and			
			subsequently			
			transferred in			
			situ into the			
			ARPES			
			chamber.			
	FeSe/ST	in situ	Starting from	Potassium	Annealing	Angle-
	O	potassium	a sample	(K)	at 350°C	resolved
	monolay	deposition	annealed at		for 20 h,	photoemissi
	er		350°C for 20		in situ	on
			79			

		h, potassium		potassium	spectroscop
		atoms are		deposition	y (ARPES),
		deposited in		, low	He
		situ onto the		temperatur	discharge
		surface of the		e (14 K	lamp (He Ia
		FeSe/STO		and 70 K)	and He II
		monolayer to		ARPES	lines),
		achieve		measurem	scanning
		higher		ents	tunneling
		electron			microscopy
		doping levels.			1 7
		The electron			
		concentration			
		increases			
		from 0.164			
		electrons per			
		unit cell in			
		the pristine			
		sample to			
		0.212 and			
		0.214 after			
		successive			
		rounds of K			
		deposition.			
		The process is			
		monitored			
		using angle-			
		resolved			
		photoemissio			
		n			
		spectroscopy			
		(ARPES) to			
		observe the			
		evolution of			
		the Fermi			
		surface (FS)			
		and band			
		structure.			
FeSe	standard	The	Not	Low	Angle-
bulk	synthesis	superconducti	specified	temperatur	resolved
crystals		vity of FeSe		e (14 K)	photoemissi
		bulk crystals		ARPES	on
		is studied		measurem	spectroscop
		using angle-		ents	y (ARPES)
		80			-

		resolved			
		photoemissio			
		n			
		spectroscopy			
		(ARPES) and			
		compared to			
		the			
		monolayer			
		films. The FS			
		of FeSe bulk			
		crystals is			
		distinct from			
		the			
		monolayer			
		films, lacking			
		the doubly			
		degenerate			
		electron-like			
		pockets at the			
		M point.			
AxFe2	potassium	Potassium is	Potassium	Electron	Angle-
ySe2	doping	used to dope	(K)	doping,	resolved
		electron		1	1 4
				low	photoemissi
		carriers into		temperatur	on
		carriers into AxFe2 ySe2,		temperatur e (14 K)	-
		carriers into AxFe2 ySe2, leading to a		temperatur	on spectroscop y (ARPES),
		carriers into AxFe2 ySe2, leading to a relatively		temperatur e (14 K)	on spectroscop y (ARPES), band
		carriers into AxFe2 ySe2, leading to a relatively high		temperatur e (14 K) ARPES	on spectroscop y (ARPES),
		carriers into AxFe2 ySe2, leading to a relatively high superconducti		temperatur e (14 K) ARPES measurem	on spectroscop y (ARPES), band
		carriers into AxFe2 ySe2, leading to a relatively high superconducti ng critical		temperatur e (14 K) ARPES measurem	on spectroscop y (ARPES), band
		carriers into AxFe2 ySe2, leading to a relatively high superconducti ng critical temperature		temperatur e (14 K) ARPES measurem	on spectroscop y (ARPES), band
		carriers into AxFe2 ySe2, leading to a relatively high superconducti ng critical temperature (Tc). The		temperatur e (14 K) ARPES measurem	on spectroscop y (ARPES), band
		carriers into AxFe2 ySe2, leading to a relatively high superconducti ng critical temperature (Tc). The exact		temperatur e (14 K) ARPES measurem	on spectroscop y (ARPES), band
		carriers into AxFe2 ySe2, leading to a relatively high superconducti ng critical temperature (Tc). The exact mechanism of		temperatur e (14 K) ARPES measurem	on spectroscop y (ARPES), band
		carriers into AxFe2 ySe2, leading to a relatively high superconducti ng critical temperature (Tc). The exact mechanism of superconducti		temperatur e (14 K) ARPES measurem	on spectroscop y (ARPES), band
		carriers into AxFe2 ySe2, leading to a relatively high superconducti ng critical temperature (Tc). The exact mechanism of superconducti vity		temperatur e (14 K) ARPES measurem	on spectroscop y (ARPES), band
		carriers into AxFe2 ySe2, leading to a relatively high superconducti ng critical temperature (Tc). The exact mechanism of superconducti vity enhancement		temperatur e (14 K) ARPES measurem	on spectroscop y (ARPES), band
		carriers into AxFe2 ySe2, leading to a relatively high superconducti ng critical temperature (Tc). The exact mechanism of superconducti vity enhancement is studied		temperatur e (14 K) ARPES measurem	on spectroscop y (ARPES), band
		carriers into AxFe2 ySe2, leading to a relatively high superconducti ng critical temperature (Tc). The exact mechanism of superconducti vity enhancement is studied using ARPES		temperatur e (14 K) ARPES measurem	on spectroscop y (ARPES), band
		carriers into AxFe2 ySe2, leading to a relatively high superconducti ng critical temperature (Tc). The exact mechanism of superconducti vity enhancement is studied using ARPES and band		temperatur e (14 K) ARPES measurem	on spectroscop y (ARPES), band
		carriers into AxFe2 ySe2, leading to a relatively high superconducti ng critical temperature (Tc). The exact mechanism of superconducti vity enhancement is studied using ARPES and band calculations.		temperatur e (14 K) ARPES measurem ents	on spectroscop y (ARPES), band calculations
(Li,Fe)O	liquid-	carriers into AxFe2 ySe2, leading to a relatively high superconducti ng critical temperature (Tc). The exact mechanism of superconducti vity enhancement is studied using ARPES and band calculations. The	Not	temperatur e (14 K) ARPES measurem ents	on spectroscop y (ARPES), band calculations
(Li,Fe)O HFeSe	liquid- gating technique	carriers into AxFe2 ySe2, leading to a relatively high superconducti ng critical temperature (Tc). The exact mechanism of superconducti vity enhancement is studied using ARPES and band calculations.	Not specified	temperatur e (14 K) ARPES measurem ents	on spectroscop y (ARPES), band calculations

(Li,Fe)OHFe	liquid-	on
Se is	gating,	spectroscop
enhanced	low	y (ARPES)
through the	temperatur	
use of a	e (14 K)	
liquid-gating	ARPES	
technique in	measurem	
the bulk. The	ents	
material is		
studied using		
ARPES to		
understand		
the electronic		
structure and		
superconducti		
ng properties.		